Valerio Olevano
TDDFT, Excitations and Spectroscopy

Applications to optical, electron and X-ray spectroscopy

in *Structures on Different Time Scales*, p. 101, De Gruyter, Berlin, 2018

Introduction

Density-functional theory (DFT) is the today condensed matter reference to calculate from first principles ground-state properties, in particular the static atomic structure. Time-dependent density-functional theory (TDDFT) is an extension of DFT to address excited-state properties, dynamics, and spectroscopy. TDDFT is an in principle exact theory to calculate *ab initio* electronic neutral excitations, as sampled in optical or energy-loss spectra. However, like in DFT, the exchange-correlation functional, a fundamental ingredient of the theory, is unknown. We must resort to approximations, and the local-density approximation (LDA) has less validity than in DFT, in particular on optical spectra in insulators. We here provide a simplified review of the fundamental aspects of the theory, theorems, frameworks, basic equations, and standard approximations, referring to the literature for more in-depth analysis. The main focus is rather on the applications where TDDFT revealed more successful: excitations and time-dependent electronic and ionic dynamics in atoms and molecules, optical absorption, electron energy-loss spectroscopy (EELS), and inelastic X-ray scattering (IXSS) in solids and nanosystems. Thanks to a continuous comparison with the experiment, the review critically assesses TDDFT standard approximations, advantages and drawbacks, reporting on some recent progresses and current challenges. TDDFT has achieved an overall good agreement with the experiment, allowing, on one hand, the interpretation of experimental spectra in terms of elementary excitations and the comprehension of the mechanisms driving physical, chemical, and even biological processes; on the other hand, *ab initio* TDDFT can today predict spectroscopic and dielectric properties with interesting returns in materials science.

Valerio Olevano: Institute Néel, CNRS and Université de Grenobles Alpes, 25 avenue des Martyrs, 38042 Grenoble, France, e-mail: valerio.olevano@neel.cnrs.fr

1 From DFT to TDDFT: electronic excitations

In the previous chapter, we have seen how the formidable many-body problem in condensed matter, can be very efficiently tackled by density-functional theory (DFT) [1, 2]. The electronic density $\rho(\mathbf{r})$ is the minimal degree of freedom needed to fully determine any static property of a condensed matter system. DFT is an in principle exact theory to calculate all ground-state properties, *e.g.*, the atomic structure, the total energy, etc., with an accuracy that depends on the approximation done on the exchange-correlation functional.

Although a very successful theory, DFT has its limits. Static DFT and the static ground-state density $\rho(\mathbf{r})$ is not sufficient to describe the dynamics and the excitation of a system in response to an applied external time-dependent perturbation $\delta v(\mathbf{r}, t)$. For example, in an energy-loss experiment, where electrons of charge $q = -e$ are shot at velocity $\mathbf{v}$ to a condensed matter system, the perturbation is the time-dependent external Coulomb potential

$$\delta v(\mathbf{r}, t) = \frac{q}{|\mathbf{r} - \mathbf{v}t|}.$$

In an optical experiment, the time-dependent external perturbation can be a laser pulse or any generic transverse electromagnetic wave in the optical limit,

$$\delta v(\mathbf{r}, t) = (\mathbf{e} \cdot \mathbf{r}) D_0 f(t) \sin(\omega t),$$

where ω is the light frequency, $\mathbf{e}$ is its polarization, D_0 is the amplitude, and $f(t)$ is the laser pulse envelope. (Unless not evident from the context, we will omit in what follows vectorial bold notation like, *e.g.*, in $\mathbf{r}$). These and other possible time-dependent perturbations cannot be accounted by DFT.

Time-dependent density-functional theory (TDDFT) is an extension of DFT that allows us to describe excited state properties, excitations, and spectroscopy. The exceedingly difficult task of calculating the wavefunction $\Psi(r_1, \ldots, r_N, t)$ of many interacting particles by direct solution of the many-body time-dependent Schrödinger equation

$$i\partial_t \Psi(r_1, \ldots, r_N, t) = H(r_1, \ldots, r_N, t)\Psi(r_1, \ldots, r_N, t), \tag{1}$$

is replaced by the simpler problem of calculating the time-dependent electronic density $\rho(r, t)$, a function of only one space variable r, with evident reduction of the degrees of freedom. The time-dependent density alone,

$$\rho(r, t) = \int dr_2 \ldots dr_N \, |\Psi(r, r_2, \ldots, r_N, t)|^2, \tag{2}$$

is a sufficient degree of freedom to fully describe the response of a system to the time-dependent perturbation. This is the thesis of the Runge–Gross theorem [3] (Section 2), an extension of the DFT Hohenberg–Kohn theorem to the time-dependent case.

In parallel to DFT, it is also possible to solve TDDFT by introduction of a fictitious auxiliary noninteracting Kohn–Sham system, constructed to provide the exact density of the real system. The density and all other observables can be calculated by solving the time-dependent independent-particle Kohn–Sham equations [4] (Section 3). The original system-size exponential scaling of the full many-body Schrödinger equation is replaced in TDDFT by a much more favorable scaling. TDDFT can in principle access the same system sizes as DFT, solids, molecules, up to nano- and biological systems, complementing ground-state with excited-state studies.

Whenever the applied time-dependent external perturbation is small with respect to the external static potential, *e.g.*, due to the nuclei, perturbation theory can be applied on top of DFT. The system undergoes a little depart from ground state and equilibrium, and TDDFT can be formulated in linear response from static DFT (Section 4). This is the situation occurring in the most spread experimental techniques, probing the response of a system to a perturbation like electron beams (electron energy-loss spectroscopy or EELS), light or weak lasers (optical absorption spectroscopy, ellipsometry, etc.), or X-rays (X-ray absorption, inelastic X-ray scattering spectroscopy, or IXSS). This is also the situation addressed by the vast majority of TDDFT applications, aiming at the calculation of excitation energies and spectra. Here TDDFT has provided the most impressive successes, achieving almost quantitative accuracies on, for example, EELS and IXSS spectroscopies already at the lowest levels of approximation.

The development of more intense laser sources, together with the possibility to study the evolution of a system out of equilibrium in pump-and-probe geometries, has opened promising applications of TDDFT beyond the linear response regime. Here, in parallel to experimental challenges, theory has in front the challenge of developing approximations more suitable to the nonperturbative regime; the challenge of developing more complete formalisms, for example, allowing the access to coupled electron–ion dynamics for applications to photo-explosion or photo-chemistry, as those illustrated in the next chapter on time-resolved X-ray diffraction (TRXRD); or a TDDFT formalism to address electronic quantum transport in nano- and molecular electronics devices [5].

2 The Runge–Gross theorem

The DFT Hohenberg–Kohn theorem proves a one-to-one correspondence between a static external potential $v(r)$, for instance, the Coulomb potential of nuclei, and the static ground-state density $\rho(r)$,

$$v(r) \Leftrightarrow \rho(r). \tag{3}$$

This is sufficient if we are only interested in the ground-state, but not sufficient if we want to study the excitation, the response of the system to an external perturbation, such as an incident electromagnetic wave switched on at an initial time t_0. The extra complication is that the external perturbation is in general represented by a time-dependent external potential $\delta v(r, t)$. The total external potential acting on the system, which is the sum of the static external potential due to the nuclei and the external perturbation,

$$v(r, t) = v(r) + \delta v(r, t), \tag{4}$$

depends on time. Since the Hohenberg–Kohn theorem, Eq. (3), only holds between static potentials and densities, DFT does not apply. To describe the system excitation, we should go beyond DFT, toward the formulation of a time-dependent theory.

The rigorous foundation of time-dependent density-functional theory is the Runge–Gross theorem [3], an extension of the Hohenberg–Kohn theorem to the time-dependent case. The Runge–Gross theorem states a one-to-one correspondence between the external time-dependent potential $v(r, t)$ and the *time-dependent* density $\rho(r, t)$. However, the formulation of the theorem is not as straightforward as the Hohenberg–Kohn theorem, Eq. (3). First, the density is in a one-to-one correspondence with the class of external potentials given by $v(r, t) + \alpha(t)$ with an arbitrary merely time-dependent function $\alpha(t)$. This issue is not peculiar to TDDFT. The addition of a pure time-dependent function $\alpha(t)$ to the external potential and to the total Hamiltonian in the full time-dependent Schrödinger equation (1) reflects in an uninfluential merely time-dependent phase factor on the full wavefunction, $\Psi(t) \to \Psi'(t) = e^{-i\alpha(t)}\Psi(t)$. Observables do not depend on the wavefunction time-dependent phase factor $e^{-i\alpha(t)}$. Second, the time-dependent external potential is in one-to-one correspondence with the time-dependent density *and* a fixed initial state $\Psi_0 = \Psi(t_0)$. The initial state is a boundary condition necessary also to fix the solution to the original first-degree differential Schrödinger equation (1). The Runge–Gross theorem can be finally mathematically formulated as

$$v(r, t) + \alpha(t) \overset{\Psi_0}{\Longleftrightarrow} \rho(r, t). \tag{5}$$

For a given system, say of N electrons with their fixed form of kinetic and many-body interaction Hamiltonians, the external potential is the only remaining degree of freedom. Once fixed the external potential and the initial state, every observable O is determined. Thanks to the stated one-to-one correspondence, the Runge–Gross theorem has the important corollary that every observable is a *unique functional* of the time-dependent density (and of the initial state):

$$O(t) = O[\rho, \Psi_0](t). \tag{6}$$

So, knowledge of the time-evolution of the density $\rho(r, t)$ can give access to the value of an observable, provided that its functional form is known, without passing by

the complex many-body wavefunction and the solution of the full time-dependent Schrödinger equation (1).

Relying on the Runge–Gross theorem, it becomes possible to build a time-dependent density-functional theory in analogy to static DFT based on the Hohenberg–Kohn theorem. The variational principle, which holds in DFT for the energy functional $E[\rho] = \langle \Psi | H | \Psi \rangle$ whose minimum, $\delta E[\rho]/\delta \rho(r,t) = 0$, occurs at the ground-state density, can be extended also to TDDFT. Since TDDFT is a time-dependent theory, instead of focussing on the energy, we need to introduce the action

$$A[\rho] = \int\limits_{t_0}^{t_1} dt \left\langle \Psi(t) \middle| i\partial_t - H(t) \middle| \Psi(t) \right\rangle.$$

The stationary points of the action, $\delta A[\rho]/\delta \rho(r,t) = 0$, provide the exact time-dependent density $\rho(r,t)$. A possible resolution scheme for TDDFT can rely on the variational principle: by varying the action and searching for the stationary points we can get the exact time-dependent density of the system.

At this point, we shold mention some difficulties with the Runge–Gross theorem. **Dependence on the initial state:** the dependence on the initial state Ψ_0 is a remarkable complication with respect to static DFT, where observables are functionals of the density alone. This dependence implies that we still have to deal with many-body wavefunctions $\Psi_0(r_1, \ldots, r_N)$ and at least with the solution of the time-independent Schrödinger equation at the initial time, although just only to fix a boundary condition. However, supposing to start from the ground state as initial state and in systems presenting a nondegenerate ground-state, the latter is a unique functional of the static ground-state density alone, $\Psi_0 = \Psi_0[\rho_0]$, by the classical Hohenberg–Kohn theorem. Observables are in this case functionals of the density alone even in the time-dependent evolution. On the other hand, an initial state not chosen to be the ground state would allow us to describe the sudden switch-on of the perturbation, which otherwise could not be covered by the Runge–Gross theorem, and this constitutes the second problem.

Limits of the Runge–Gross theorem: the Runge–Gross theorem has been demonstrated for a much more restricted domain of validity than the Hohenberg–Kohn theorem. The original Runge–Gross demonstration relies on the hypothesis that the external potential $v(r,t)$ is analytic at the initial time t_0, that is, all time derivatives $\partial^n v/\partial t^n$ exist at t_0, so that $v(r,t)$ admits a Taylor expansion in t_0. This excludes many possibilities, among them the adiabatical switch-on. However, though a general proof of the Runge–Gross theorem for arbitrary time-dependent potentials $v(r,t)$ does not exist [6], the theorem has been extended in the following years to other classes of potentials, so that we may hope that it is more general than actually demonstrated. In particular, the validity of the theorem has been extended significantly for small perturbations [7, 8] in the linear response regime, the most important for TDDFT applications.

v-representability problem: like in DFT and for the Hohenberg–Kohn theorem, the Runge–Gross theorem states the uniqueness of the potential corresponding to a density. However, it does not state its existence. There can exist densities that do not correspond to any potential [9]. This can be a problem when varying functionals with respect to arbitrary densities. It can become more critical for the existence of a Kohn–Sham system, as we will see in the next section.

3 Time-dependent Kohn–Sham equations

The Runge–Gross theorem states that any observable is a unique functional of the density. However, like in DFT, finding an explicit form of functionals can be rather difficult. This is in particular true for the kinetic energy functional and motivates the introduction of a Kohn–Sham scheme also in TDDFT.

The proof of the Runge–Gross theorem is independent from the form of the many-body interaction between the particles. In particular, the theorem is also valid in the case of noninteracting particles. Provided that the density is *noninteracting v-representable*, there exists an unique potential associated with it. Thus we can solve TDDFT by a Kohn–Sham scheme like in DFT. A Kohn–Sham fictitious non-interacting system is introduced such that, by construction, it provides exactly the same density $\rho(r,t)$ of the real interacting system. The potential associated with this system is called the Kohn–Sham potential $v^{\mathrm{KS}}(r,t)[\rho]$, and it is a functional of the density (and of the noninteracting system initial state $\Phi_0 = \Phi(t=0)$). We can solve the Kohn–Sham system by solving an easier single-particle Schrödinger equation. With respect to static DFT, the TDDFT Kohn–Sham equation is a time-dependent Schrödinger-like equation

$$i\partial_t \phi_i^{\mathrm{KS}}(r,t) = \left[-\frac{1}{2}\partial_r^2 + v^{\mathrm{KS}}(r,t) \right] \phi_i^{\mathrm{KS}}(r,t), \qquad (7)$$

where $\phi_i^{\mathrm{KS}}(r,t)$ are the Kohn–Sham wavefunctions. The density can be calculated by a sum over Kohn–Sham wavefunctions of all occupied states:

$$\rho(r,t) = \sum_i^{\mathrm{occ}} |\phi_i^{\mathrm{KS}}(r,t)|^2. \qquad (8)$$

As in the static DFT case, it is convenient to split the Kohn–Sham potential into three terms:

$$v^{\mathrm{KS}}[\rho](r,t) = v(r,t) + v_{\mathrm{H}}[\rho](r,t) + v_{\mathrm{xc}}[\rho](r,t), \qquad (9)$$

with an external potential v, a Hartree potential

$$v_{\mathrm{H}}[\rho](r,t) = \int dr' \, \frac{\rho(r',t)}{|r-r'|}, \qquad (10)$$

and an exchange-correlation potential

$$v_{\mathrm{xc}}[\rho](r,t) = \frac{\delta A_{\mathrm{xc}}[\rho]}{\delta\rho(r,t)} \tag{11}$$

related to the exchange-correlation action $A_{\mathrm{xc}}[\rho]$. Like in DFT, the latter is unknown and needs to be approximated.

When following the Kohn–Sham scheme, we run into further difficulties.

Noninteracting v-representability problem: as already mentioned, the v-representability becomes a more serious problem within the Kohn–Sham scheme. A real density ρ, corresponding to a real external potential v, may *not* be noninteracting v-representable, *i.e.*, it may be that this density ρ is not a solution of a noninteracting system and does not correspond to some Kohn–Sham potential v^{KS}. In this case, the Kohn–Sham system does not exist, and the Kohn–Sham resolution scheme is not viable. The question of the noninteracting and interacting v-representabilities, has been analyzed extensively [10, 11, 6, 12] but still keeps open.

Symmetry-causality paradox: the response function $\delta v_{\mathrm{xc}}[\rho](r,t)/\delta\rho(r',t')$, called the exchange-correlation kernel and denoted $f_{\mathrm{xc}}[\rho](r,t,r',t')$, as we will see in Section 4, must be *causal*, that is, $f_{\mathrm{xc}}(t,t') = 0$ for all $t' > t$, implying that the density changes $\delta\rho(t')$ at later times $t' > t$ cannot affect the exchange-correlation potential at earlier times. But from Eq. (11) we could write $f_{\mathrm{xc}}[\rho](r,t,r',t') = \delta^2 A_{\mathrm{xc}}[\rho]/\delta\rho(r,t)\delta\rho(r',t')$, which is *symmetric* in t and t' in contrast to its causality. This is the so called symmetry-causality paradox. The paradox is related to the fact that TDDFT is inherently an out-of-equilibrium theory. The application of a time-dependent perturbation inevitably brings the system out of equilibrium. Formulation of TDDFT as a truly out-of-equilibrium theory within a Keldysh formalism [13] solves the paradox.

4 TDDFT in linear response

An important simplification of the theory is achieved when working in the linear response regime [4, 14, 15, 16, 17, 18]. Suppose that we can split the time-dependent external potential into a purely static term (to be identified, as usual, with the potential generated by the positive nuclei or ions) and a time-dependent perturbation term, as in Eq. (4):

$$v(r,t) = v(r) + \delta v(r,t)$$

with a time-dependent perturbation term, which is off before an initial time t_0, $\delta v(r,t) = 0$ for all $t < t_0$, and which is in particular much smaller than the static term,

$$\delta v(r,t) \ll v(r). \tag{12}$$

Then the theory can be factorized into an ordinary static density-functional theory plus a linear response theory to the small time-dependent perturbation. In this case the Hohenberg–Kohn and Runge–Gross theorems together state that the linear response time-dependent variation to the density is one-to-one with the time-dependent perturbation to the external potential,

$$\delta\rho(r,t) \Leftrightarrow \delta v(r,t).$$

Condition (12) is usually satisfied when considering normal situations referring to condensed matter systems submitted to small excitation. This is the case in optical spectroscopy using ordinary light, energy-loss spectroscopy, or X-ray spectroscopies. On the other hand, for spectroscopies implying strong electromagnetic fields, intense lasers, etc., condition (12) does not hold anymore, and the situation cannot be described by linear-response TDDFT.

A linear-response TDDFT (LR-TDDFT) calculation is a two-step procedure: starting from the static ionic external potential $v(r)$, we perform an ordinary static DFT calculation of the Kohn–Sham energies ϵ_i^{KS} and wavefunctions $\phi_i^{\mathrm{KS}}(r)$, and so of the ground-state electronic density $\rho(r)$; then we do a linear-response TDDFT calculation of the density variation $\delta\rho(r,t)$ corresponding to the external time-dependent perturbation $\delta v(r,t)$. From $\delta\rho(r,t)$ we can then calculate the *polarizability* χ of the system defined as the linear response proportionality coefficient $\delta\rho = \chi\delta v$ of the density with respect to the external potential,

$$\delta\rho(x_1) = \int dx_2 \, \chi(x_1,x_2)\delta v(x_2), \tag{13}$$

where we have used the notation x for the space and time variables, $x = \{r,t\}$, possibly including also the spin index, $x = \{r,t,\sigma\}$. For the remainder of the chapter, when it will be clear from context, we will simplify the notation omitting convolution products $\int dx$ as in Eq. (13).

It is possible to follow a Kohn–Sham scheme also in linear-response TDDFT. A fictitious noninteracting Kohn–Sham (KS) system is introduced under the hypothesis that its density response $\delta\rho^{\mathrm{KS}}$ is equal to the density response of the real system, $\delta\rho = \delta\rho^{\mathrm{KS}}$, but in response to an effective (Kohn–Sham) perturbation,

$$\delta v^{\mathrm{KS}}(x) = \delta v(x) + \delta v_{\mathrm{H}}(x) + \delta v_{\mathrm{xc}}(x), \tag{14}$$

composed of the real external perturbation $\delta v(x)$ plus the Hartree term

$$\delta v_{\mathrm{H}}(x_1) = \int dx_2 \, w(x_1,x_2)\delta\rho(x_2) \tag{15}$$

and the exchange-correlation term

$$\delta v_{\mathrm{xc}}(x_1) = \int dx_2 \, f_{\mathrm{xc}}[\rho](x_1,x_2)\delta\rho(x_2) \tag{16}$$

with the instantaneous static Coulomb interaction

$$w(x_1, x_2) = \frac{1}{|r_2 - r_1|} \delta(t_1, t_2)$$

and

$$f_{\text{xc}}[\rho](x_1, x_2) = \frac{\delta v_{\text{xc}}[\rho](x_1)}{\delta \rho(x_2)},$$

which is called the *exchange-correlation kernel* and is the fundamental quantity in linear-response TDDFT and, at the same time, the big unknown of the theory. We will consider it again all over the rest of this chapter and in particular in Sections 6, 13, and 14 to provide approximations to it, evaluate their performances and drawbacks, and study possible improvements.

For the fictitious KS independent particle system, we can introduce the corresponding *Kohn–Sham polarizability* χ^{KS} by

$$\delta\rho(x_1) = \int dx_2 \, \chi^{\text{KS}}(x_1, x_2) \delta v^{\text{KS}}(x_2), \tag{17}$$

that is, the polarizability of the independent-particle system that responds to the external perturbation δv^{KS} by the density variation $\delta\rho$. By applying perturbation theory to the Kohn–Sham equation (7) it can be shown that the Kohn–Sham polarizability is provided by the Adler–Wiser [19, 20] analytic expression

$$\chi^{\text{KS}}(r_1, r_2, \omega) = \sum_{i,j} \left(f_i^{\text{KS}} - f_j^{\text{KS}} \right) \frac{\phi_j^{\text{KS}}(r_1)\phi_i^{\text{KS}\,*}(r_1)\phi_i^{\text{KS}}(r_2)\phi_j^{\text{KS}\,*}(r_2)}{\omega - (\epsilon_j^{\text{KS}} - \epsilon_i^{\text{KS}}) + i\eta}, \tag{18}$$

where ϵ_i^{KS} are the DFT Kohn–Sham energies, $\phi_i^{\text{KS}}(r)$ are the respective wavefunctions, and f_i^{KS} are their occupation numbers (η is an infinitesimal introduced to have well-defined Fourier transforms, $\chi(\tau = t_2 - t_1) \to \chi(\omega)$, for polarizabilities and other response functions). The Kohn–Sham polarizability can hence be calculated once we have solved the static DFT Kohn–Sham problem. By combining Eqs. (13), (17), and (14) we can express the polarizability χ of the real system in a Dyson-like form

$$\chi = \chi^{\text{KS}} + \chi^{\text{KS}}(w + f_{\text{xc}})\chi \tag{19}$$

or also in an explicit form

$$\chi = (1 - \chi^{\text{KS}}w - \chi^{\text{KS}}f_{\text{xc}})^{-1}\chi^{\text{KS}} \tag{20}$$

in terms of the Kohn–Sham polarizability χ^{KS} and of the unknown exchange-correlation kernel f_{xc}. So, once we have an expression for the kernel, it is relatively easy to calculate, within LR-TDDFT, the full polarizability χ of the real system.

The polarizability χ is a fundamental quantity of any condensed matter system. It directly contains the excitation energies of the system, as we will see in Section 5. In Section 7, we will see that χ is directly related to the dielectric function and

so to optical spectroscopy, EELS, and other experimental observables and spectra. The macroscopic dielectric function also enters into Maxwell equations in matter. So, knowledge of the polarizability or, equivalently, of the dielectric function fully determines the dielectric properties of a condensed matter system. In nonmagnetic systems, the dielectric polarizability is alone sufficient to fully determine the behavior of matter under electromagnetic fields.

5 Excitation energies

To study excitations or to have direct access to spectroscopy, it is convenient to pass from the time space to the frequency ω-space. After Fourier transform, all the convolution products in time space, like the definition of the polarizability Eq. (13), become direct products in frequency space,

$$\delta\rho(\omega) = \chi(\omega)\delta v(\omega).$$

From the latter expression we can see that the frequencies ω_l where the polarizability χ diverges correspond to the resonances, self-sustained modes of the system. These frequencies are the excitation energies of the system and can be extracted from the analytic structure of the polarizability by looking for the poles ω_l of the full polarizability χ. These are different from the poles of the zeroth-order Kohn–Sham polarizability χ^{KS}, which, as we can see from Eq. (18), correspond to the differences between the static DFT Kohn–Sham eigenvalues, $\omega_t^{\mathrm{KS}} = \epsilon_j^{\mathrm{KS}} - \epsilon_i^{\mathrm{KS}}$. By introducing a compact Hartree plus exchange-correlation kernel $f_{\mathrm{Hxc}} = w + f_{\mathrm{xc}}$ in Eq. (20),

$$\chi = (1 - \chi^{\mathrm{KS}} f_{\mathrm{Hxc}})^{-1} \chi^{\mathrm{KS}}, \tag{21}$$

we can see that the inverse operator $(1 - \chi^{\mathrm{KS}} f_{\mathrm{Hxc}})^{-1}$ has the task to bring the poles of its right operand χ^{KS}, that is, the excitations of the Kohn–Sham fictitious noninteracting system, to the poles of the full polarizability χ, that is, the excitations of the real system. Rewriting Eq. (21) as

$$\left[1 - \chi^{\mathrm{KS}}(\omega) f_{\mathrm{Hxc}}(\omega)\right] \chi(\omega) = \chi^{\mathrm{KS}}(\omega), \tag{22}$$

and neglecting its real space r, r' structure, we can see that the poles ω_l of $\chi(\omega)$ must correspond to the zeros of the term $[1 - \chi^{\mathrm{KS}}(\omega) f_{\mathrm{Hxc}}(\omega)]$ for the right-hand side of the equation, $\chi^{\mathrm{KS}}(\omega)$, to remain finite at ω_l. More rigorously, the true excitation energies ω_l are precisely those frequencies where the eigenvalues of the integral operator $[1 - \chi^{\mathrm{KS}}(\omega) f_{\mathrm{Hxc}}(\omega)]$ vanish. Therefore, the search for the excitation energies of the real system can be recast into an eigensystem problem. After some algebra, the true excitation energies can be calculated as the eigenvalues ω_l of the matrix equation

$$\begin{pmatrix} A & B \\ B^* & A^* \end{pmatrix} \begin{pmatrix} X \\ Y \end{pmatrix} = \omega_l \begin{pmatrix} 1 & 0 \\ 0 & -1 \end{pmatrix} \begin{pmatrix} X \\ Y \end{pmatrix}, \tag{23}$$

where

$$
\begin{aligned}
A_{tt'} &= \omega_t^{\mathrm{KS}}\delta_{tt'} + 2\int dr dr'\, \rho_t^{\mathrm{KS}*}(r)f_{\mathrm{Hxc}}(r,r')\rho_{t'}^{\mathrm{KS}}(r'), \\
B_{tt'} &= 2\int dr dr'\, \rho_t^{\mathrm{KS}*}(r)f_{\mathrm{Hxc}}(r,r')\rho_{-t'}^{\mathrm{KS}}(r'), \\
\omega_t^{\mathrm{KS}} &= \epsilon_j^{\mathrm{KS}} - \epsilon_i^{\mathrm{KS}}, \\
\rho_t^{\mathrm{KS}}(r) &= \phi_i^{\mathrm{KS}*}(r)\phi_j^{\mathrm{KS}}(r).
\end{aligned}
$$

We can also consider a quadratic form of Eq. (23),

$$
MF_l = \omega_l^2 F_l, \tag{24}
$$

or can also consider an approximation, known as the Tamm–Dancoff approximation (TDA), consisting in the neglect of the coupling B matrix, $B = 0$.

Eq.s (23) and (24), known in chemistry as the Casida equations [21, 22, 23, 24] allow us to directly calculate the excitation energies ω_l of a finite system, like a molecule or an atom. We will see in Section 9 an application of these equations to the calculation of the excitations in the helium atom. On this system, in Fig. 1, we will compare the starting DFT Kohn–Sham energy differences ω_t^{KS} and the final TDDFT excitation energies ω_l obtained as solutions of Eq. (23) or (24) to the exact excitation energies obtained by an exact Hylleraas-like calculation [25] or measured with high-accuracy experiments in helium.

We can also calculate the oscillator strength associated with the excitation ω_l from the eigenvector F_l or $(X\,Y)$. Physically, an oscillator strength can be interpreted as the probability for the system to make the transition to the excited state, exactly like the Einstein coefficients of time-dependent perturbation theory and Fermi's golden rule in noninteracting systems, *e.g.*, the hydrogen atom. An oscillator strength equal to zero indicates a forbidden transition.

6 RPA and ALDA exchange-correlation kernel approximations

As we anticipated in Section 4, TDDFT would be an exact theory if we knew the exact density-functional form of the exchange-correlation term. Like in DFT, this term has to be approximated. The most common approximations for the exchange-correlation kernel f_{xc} are the *random-phase approximation* (RPA) and the *adiabatic local-density approximation* (indicated as ALDA or TDLDA). In the RPA approximation the exchange-correlation kernel is set to zero, $f_{\mathrm{xc}} = 0$, and exchange-correlation effects are neglected. This is not such a crude approximation as we might think. Indeed, exchange-correlation effects are neglected only in the linear response

to the external perturbation, but not in the previous static DFT calculation, where they were taken into account by choosing an appropriate exchange-correlation potential v_{xc} in LDA or GGA for example. Later we will see examples of the validity of this approximation.

In the adiabatic local-density approximation, the kernel is taken to be

$$f_{xc}^{\mathrm{ALDA}}(x_1, x_2) = \frac{\delta v_{xc}^{\mathrm{LDA}}[\rho](x_1)}{\delta \rho(x_2)} = \delta(x_1, x_2) f_{xc}^{\mathrm{HEG}}(\rho(r)), \tag{25}$$

where $f_{xc}^{\mathrm{HEG}}(\rho)$ is the exchange-correlation kernel of the homogeneous electron gas or jellium model. The ALDA kernel is a local and ω-independent static (instantaneous) approximation. As we will show, TDLDA is a good approximation to calculate EELS or IXSS and even CIXS spectra. RPA and TDLDA are however unsatisfactory for optical spectra in semiconductors and insulators, *i.e.*, spectra where electron–hole (e–h) interaction effects, giving rise to bound excitons or excitonic effects, are important. To provide new good approximations for the exchange-correlation kernel beyond ALDA and to make TDDFT work also on optical properties was the motivation of the last 10 ten-year research efforts. This is presented in the last part of this chapter.

7 Dielectric function and experimental spectra

From the polarizability we can calculate the *microscopic dielectric function* $\varepsilon(x_1, x_2)$,

$$\varepsilon^{-1} = 1 + w\chi. \tag{26}$$

Observable quantities and spectra are related to the *macroscopic dielectric function* ε_{M}, obtained from the microscopic ε by spatially averaging over a distance large enough with respect to the microscopic structure of the system (*e.g.*, an elementary cell in periodic crystalline solids):

$$\varepsilon_{\mathrm{M}}(r, r', \omega) = \overline{\varepsilon(r, r', \omega)}. \tag{27}$$

It can be shown that in solids the operation of averaging corresponds to the reciprocal space expression

$$\varepsilon_{\mathrm{M}}(q, \omega) = \frac{1}{\varepsilon_{G=0,G'=0}^{-1}(q, \omega)}, \tag{28}$$

that is, the macroscopic ε_{M} is the inverse of the $G = G' = 0$ element (G and G' are reciprocal-space vectors) of the reciprocal-space *inverse* microscopic dielectric matrix ε^{-1}. This does not correspond to the $G = G' = 0$ element of the *direct* microscopic dielectric matrix ε,

$$\varepsilon_{\mathrm{M}}^{\mathrm{NLF}}(q, \omega) = \varepsilon_{G=0,G'=0}(q, \omega), \tag{29}$$

if the microscopic dielectric matrix contains off-diagonal terms. Expression (29) is an *approximation* (NLF) to the exact macroscopic dielectric function. By this approximation the so-called crystal *local-field* effects are neglected (no local-field effects, NLF). We can see that the two expressions (28) and (29) coincide for the homogeneous electron gas or jellium model. Local-field effects are absent in the homogeneous electron gas and marginal in weakly inhomogeneous systems (*e.g.*, silicon). They become important in systems presenting strong inhomogeneities in the electronic density, such as reduced dimensionality systems (2D surfaces/graphene, 1D nanotubes/wires, 0D clusters, etc.).

The macroscopic dielectric function ε_M is the key quantity to calculate observables and spectra. For example, the *dielectric constant* is given by

$$\varepsilon_\infty = \lim_{q \to 0} \varepsilon_M(q, \omega = 0). \tag{30}$$

The ordinary *optical absorption*, as measured, *e.g.*, in ellipsometry, is directly related to the imaginary part of the macroscopic dielectric function:

$$\mathrm{ABS}(\omega) = \Im \varepsilon_M(q \to 0, \omega). \tag{31}$$

Finally, the *energy-loss function*, as measured in EELS or IXSS, is related to minus the imaginary part of the inverse macroscopic dielectric function:

$$\mathrm{ELF}(q, \omega) = -\Im \varepsilon_M^{-1}(q, \omega). \tag{32}$$

8 TDDFT implementations and codes

The equations presented in the previous sections are implemented in several TDDFT codes, though not so many like in the case of DFT. TDDFT codes differ by the used basis set, *e.g.*, plane waves (PW), linearized augmented plane waves (LAPW), Gaussians, etc., like in DFT. Most importantly, there are implementations in real time-space and in frequency-reciprocal space.

The DP code [26] is a linear-response TDDFT pseudopotential code on a plane-wave basis set working in the frequency-reciprocal space, although some quantities are calculated in the frequency-real space. The code allows us to calculate dielectric and optical spectra, such as optical absorption, reflectivity, refraction indices, EELS, IXSS, and CIXS spectra. It uses periodic boundary conditions and works both on bulk 3D systems and also, by using supercells containing vacuum, on 2D surfaces, 1D nanotubes/wires, and 0D clusters and molecules. It can deal with both insulating or metallic systems. Several approximations to the exchange-correlation kernel are implemented, and local-field effects can be switched on and off.

The DP code relies on a previous DFT calculation of the KS energies and wavefunctions, provided by another PW code, for example, ABINIT [27]. The first task

is to back Fourier transform the KS wavefunctions, $\phi_i^{\mathrm{KS}}(G) \to \phi_i^{\mathrm{KS}}(r)$, from reciprocal to real space. Then `DP` calculates in real space the optical matrix elements $\rho_{ij}^{\mathrm{KS}}(r) = \phi_i^{\mathrm{KS}*}(r)\phi_j^{\mathrm{KS}}(r)$, which are Fourier transformed, $\rho_{ij}^{\mathrm{KS}}(r) \to \rho_{ij}^{\mathrm{KS}}(G)$, to reciprocal space. The next step is the calculation of the Kohn–Sham polarizability

$$\chi_{G_1 G_2}^{\mathrm{KS}}(q,\omega) = \sum_{i,j \neq i} \left(f_i^{\mathrm{KS}} - f_j^{\mathrm{KS}} \right) \frac{\rho_{ij}^{\mathrm{KS}}(G_1,q)\rho_{ij}^{\mathrm{KS}*}(G_2,q)}{\epsilon_i^{\mathrm{KS}} - \epsilon_j^{\mathrm{KS}} - \omega - i\eta}. \tag{33}$$

At this point the RPA dielectric function and spectra in the NLF approximation are already available via $\varepsilon_{\mathrm{M}}^{\mathrm{RPA\text{-}NLF}}(q,\omega) = 1 - w\chi_{00}^{\mathrm{KS}}(q,\omega)$. For approximations beyond, `DP` first calculates the polarizability χ by Eq. (20). The ALDA exchange-correlation f_{xc} is calculated in real space and then Fourier transformed in reciprocal space. At the end, `DP` calculates the dielectric function ε Eq. (26) and finally the observable macroscopic dielectric function $\varepsilon_{\mathrm{M}}(q,\omega)$ Eq. (28), including local-field effects. The dielectric function $\varepsilon_{\mathrm{M}}(q,\omega)$ is provided in an output file, both in the real and imaginary parts, as a function of ω (the BZ vector q is fixed and specified as an input parameter to the `DP` code). The most time-consuming steps are the calculation of χ^{KS}, where Fourier transforms are carried out using FFT (scaling $O(N \log N)$ instead of $O(N^2)$), and the matrix inversion to calculate χ (Eq. (20)), which is however replaced by the resolution of a linear system of equations (scaling $O(N^2)$ instead of $O(N^3)$).

An example of a linear-response TDDFT code on a LAPW basis set is `Elk` [28]. The `Elk` code works in frequency-reciprocal space and allows us to perform all-electron full-potential nonpseudopotential calculations.

A real space-time implementation of TDDFT is the `Octopus` code [29]. The real space implementation makes it particularly well suited to isolated systems (atoms, molecules, clusters, etc.), though of course with limitations on periodic systems. However, its most important feature is that it can go beyond linear-response TDDFT, thanks to the explicit evaluation of the time evolution of the density.

9 TDDFT on the simplest example: He atom

The simplest many-body interacting system in nature is the helium atom. Here many-body means just only two electrons. For this system, there are both very accurate experimental measures and theoretical calculations for the ground and excited states. It looks a toy model, but, contrary to other widespread many-body models, it is a real system with a real long-range Coulomb many-body interaction among electrons. So, it represents an important workbench model for theory because, instead of comparing directly with the experience, we can compare different many-body theories at the same nonrelativistic level of physics, *e.g.*, switching off relativistic, finite nuclear mass effects, QED radiative corrections, etc. TDDFT is an

in principle exact theory to calculate excited states, and so exact TDDFT should work also on the helium atom. A different issue is whether a given approximation within TDDFT, *e.g.*, RPA or adiabatic LDA (TDLDA), is going to provide accurate results, or at least good enough to reproduce with an acceptable approximation, or just only qualitatively, the right physics of a system.

The helium atom is a good example to show how TDDFT works in practice and what are the typical results we can get out. In the example we report here, the first step is a DFT calculation of the ground-state density and the Kohn–Sham electronic structure, both energies ϵ_i^{KS} and wavefunctions $\phi_i^{\mathrm{KS}}(r)$. Then a linear-response TDDFT calculation, Eqs. (23) and (24), is performed on top of DFT to get the neutral excitation energies, to be compared with the transition energies observed in an optical absorption experiment, and optionally also the oscillator strengths. The quality of a TDDFT calculation is affected by both steps. In particular, it is affected by both the approximation for the static exchange-correlation potential $v_{xc}(r)$, used in the ground-state DFT calculation, and also by the approximation for the exchange-correlation kernel $f_{xc}(r, r', \omega)$, used in the following linear-response TDDFT calculation. Of course, it is preferable to coherently use the same level of approximation in both steps, *e.g.*, LDA in DFT and ALDA in TDDFT, but this is not necessary. As we will see in this and following examples, the quality of a given approximation, *e.g.* LDA, not necessarily is the same in DFT and TDDFT. This depends on the system typology (*e.g.*, isolated, extended, 2D, etc.) and on the studied properties. We will rediscuss this point.

In Fig. 1 we show both a table and a diagram presenting the excitation energies of the helium atom for the lowest excited states $n^{2S+1}L$, both the singlet $S = 0$ and the triplet $S = 1$ series. The excitation energies are measured from the ground state 1^1S, which is hence set as the zero of the energies, whereas the continuum of first ionization, $\mathrm{He}^+(1s) + \mathrm{e}^-$, lies at 0.9037 Ha. The result indicated in the table and in the graph as "exact" is the accurate variational nonrelativistic calculation of Ref. [25]. It coincides with the experiment within the quoted 10^{-4} Ha accuracy. This is to be compared with the DFT and TDDFT results, the first two columns in the table and in the graph.

The helium atom is a fortunate case where the exact DFT static Kohn–Sham potential is known [30]. This is possible since we know from very accurate variational calculations [30] the full many-body wavefunction and the density of the ground state, from which we can derive the Kohn–Sham doubly occupied wavefunction, and invert the Kohn–Sham equation to get the exact Kohn–Sham potential. We can then solve the Kohn–Sham equations to find the exact Kohn–Sham energies and wavefunctions, so to have the best starting point to perform the following linear-response TDDFT calculation. In Fig. 1 we present the results of such calculation [14], done using the exact Kohn–Sham potential for the static DFT calculation and the TDLDA approximation for the linear-response TDDFT last step. These results will faithfully represent the performances of TDDFT and the TDLDA approximation, without

DFT Exact KS	TDDFT ALDA	Exact (EXP)	State
0.8836	0.8838	0.8838	5^1P
	0.8832	0.8832	5^3P
0.8819	0.8835	0.8825	5^1S
	0.8815	0.8811	5^3S
0.8722	0.8726	0.8727	4^1P
	0.8715	0.8714	4^3P
0.8688	0.8719	0.8701	4^1S
	0.8679	0.8672	4^3S
0.8476	0.8483	0.8486	3^1P
	0.8457	0.8456	3^3P
0.8392	0.8461	0.8425	3^1S
	0.8368	0.8350	3^3S
0.7772	0.7764	0.7799	2^1P
	0.7698	0.7706	2^3P
0.7460	0.7678	0.7578	2^1S
	0.7351	0.7285	2^3S
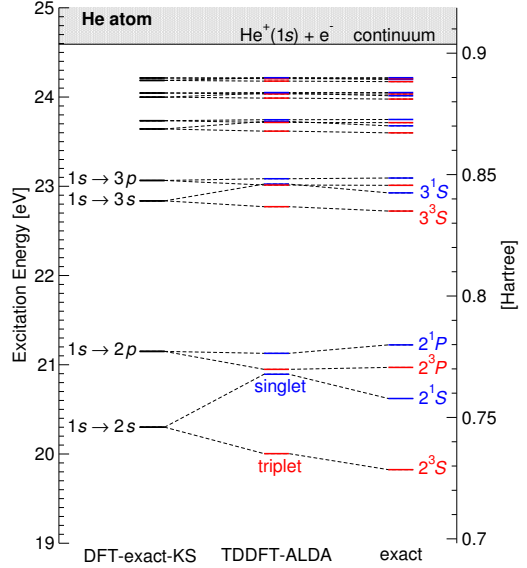
Fig. 1. Helium atom excitation energies for the lowest states $n^{2S+1}L$ with $n = 2 \to 5$, $L = S, P$, both the singlet $S = 0$ and the triplet $S = 1$ series. The 0 of the energy is set to the ground state 1^1S, so that the continuum $He^+(1s) + e^-$ is set to the ionization potential 0.9037 Ha. Left: DFT Kohn–Sham energy differences from the exact Kohn–Sham potential [30]; middle: TDDFT in the ALDA approximation [31]; right: exact nonrelativistic result [25], which, within the quoted 10^{-4} Ha accuracy, also coincides with the experiment.

being affected by approximations in the DFT first step. We first report the DFT Kohn–Sham energy differences $\omega_{ij}^{\mathrm{KS}} = \epsilon_j^{\mathrm{KS}} - \epsilon_i^{\mathrm{KS}}$ calculated using the unapproximated exact Kohn–Sham potential. Once again we stress that the DFT Kohn–Sham eigenvalues are the energies of a fictitious noninteracting system, and so they are unphysical. They cannot be interpreted as the true quasiparticle charged (addition or removal of an electron) excitation energies of the many-body interacting system, nor their difference can be interpreted as the neutral excitation energies. Nevertheless, we remark that, at least in the case of He atom, the Kohn–Sham energy differences are already surprisingly close to the exact neutral excitation energies of the system. They lie in the middle between the singlet and triplet energies, and they are a very good starting point for the next linear-response TDDFT correction. Finally, we remark that TDDFT in the adiabatic LDA reveals a very good approximation for the singlet–triplet splitting. This is a surprisingly good result also in consideration of the simplicity of the TDLDA approximation. For the highest excited states, TDLDA is in perfect quantitative agreement with the exact result. However, this is the easiest part of the spectrum for TDDFT to reproduce to. Indeed, here the singlet–triplet exchange split is small, and so the validity of the final result is above all due to the

exact DFT KS starting point. The accuracy of the DFT-TDDFT result deteriorates when going toward the lowest energy states, and here we see the limits of the ALDA approximation. In some cases, TDLDA inverts the order of states, like in the case of 3^1S and 3^3P.

We mention however that if the same LDA approximation were applied also to the first step static DFT calculation, the Kohn–Sham energy differences (starting point for the TDDFT calculation) would result much worse. Apart from only the first occupied state, the rest of the Kohn–Sham LDA energy spectrum is unbound, raised in the continuum. There is no Rydberg series in DFT Kohn–Sham LDA (or also GGA) atoms. This is due to the wrong exponential e^{-r}, instead of $1/r$, asymptotical decay of the LDA (and GGA) potential. This is a very difficult starting point for the TDDFT approximated kernel to correct. So, the surprisingly good result reproduced in Fig. 1 is just only thanks to our knowledge of the exact DFT KS potential in this system. Unfortunately, exact DFT results are only known for a few systems, mainly simple atoms.

10 TDDFT electron and ion dynamics versus TRXRD

The direct solution of the time-dependent Kohn–Sham equation (7) in real space-time allows us to follow the evolution of a system electronic density $\rho(r, t)$ after excitation by an external potential $\delta v(r, t)$. In this way, we can access the full (beyond linear) response of a system submitted to a strong perturbation and have a time-resolved study of phenomena, like the ionization of a molecule, or the breaking or the formation of chemical bonds, etc. This is a kind of studies that become more and more available from the experiment, thanks to the advent of ultrashort, femtosecond and below, laser pulses and pump-and-probe experimental setups.

Fig. 2 presents a real space-time TDLDA calculation [32] on an acetylene molecule excited by a short laser pulse. The figure presents snapshots of the time-dependent electron localization function [32, 34], a quantity related to the electron density, current, and kinetic energy density and more suited to put into evidence chemical bondings. The molecule is initially in its ground state (Fig. 2a), characterized by two blobs around the hydrogen atoms and the torus typical for a triple bond between the two carbon atoms. With the raising of the laser pulse, the electron cloud starts to oscillate until the system ionizes, as it is evident from two blobs of electrons that leave the system toward the left (Fig. 2b) and the right (Fig. 2c), with wave-packets that spread with time. Later, the central torus widens (Fig. 2d) until it breaks into two separate tori (Fig. 2e) around the two carbon atoms: this can be interpreted as the transition from the bonding π state to the antibonding π^* state. The system is left into the excited state.
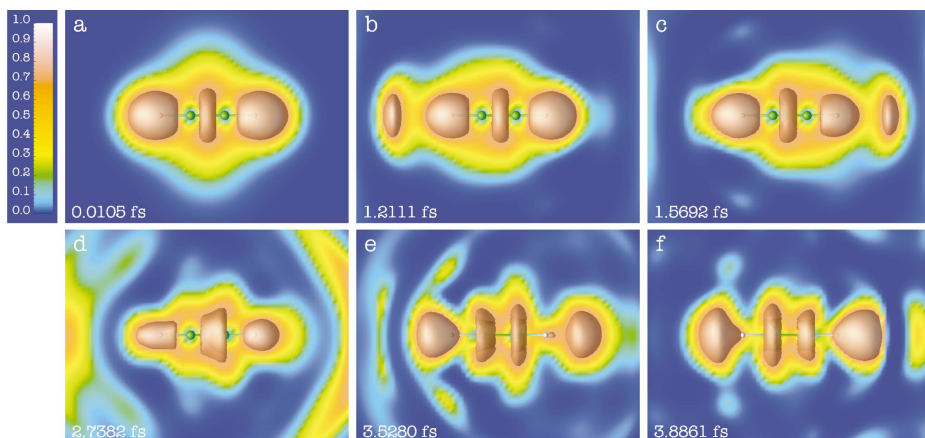
Fig. 2. Snapshots of the time-dependent electron localization (TD-ELF) for the excitation of acetylene (C_2H_2) by a laser pulse polarized along the molecular axis at frequency $\omega = 17.5$ eV, intensity $I = 1.2 \cdot 10^{14}$ W cm^{-2}, pulse duration 7 fs (reproducing Fig. 1 of Ref. [32]). The molecule is along the longitudinal axis, with the carbon atoms represented by green and the hydrogens by white balls. The sequence shows first the ionization of the molecule and then the transition from the bonding state π to the anti-bonding state π^*. The full movie can be watched at [33].

In the previous example the ions are kept fixed at their molecular ground-state equilibrium position, and only electronic degrees of freedom are let evolve along the time-dependent TDDFT dynamics. This is valid when the perturbation is small with respect to the ionic potential and so does not cause a rearrangement of the atomic structure, a chemical reaction, or the fragmentation of the molecule. However, we can also relax the constraint on the ion positions and perform a full electron and ion time-dependent TDDFT dynamics. Fig. 3 presents a real-space TDLDA dynamics [32] on an ethene molecule shot by a fast nonrelativistic proton. Fig. 3a shows the initial configuration with the proton (bottom white sphere) shot against the leftmost carbon atom (green sphere) of the molecule. While approaching the molecule, the proton is seen to dress some electronic charge (Fig. 3b). Then it is scattered and leaves the system bringing part of the electronic charge (Fig. 3c). The molecule is left into a perturbed excited state. In Fig. 3d the leftmost carbon has already broken the bonds with the two hydrogens (which are going to form a hydrogen molecule), and in Fig. 3e, we can see the formation of a lone pair above it. Finally, in Fig. 3f the molecule is completely explosed into a H_2 molecule (left) and two CH fragments, each with a characteristic lone pair near the C atom.

This kind of theoretical studies can be of real benefit in the interpretation of experiments and a valuable complement of time-resolved X-ray diffraction (TRXRD) studies, as treated in the next chapter. By TRXRD we can follow the dynamics of
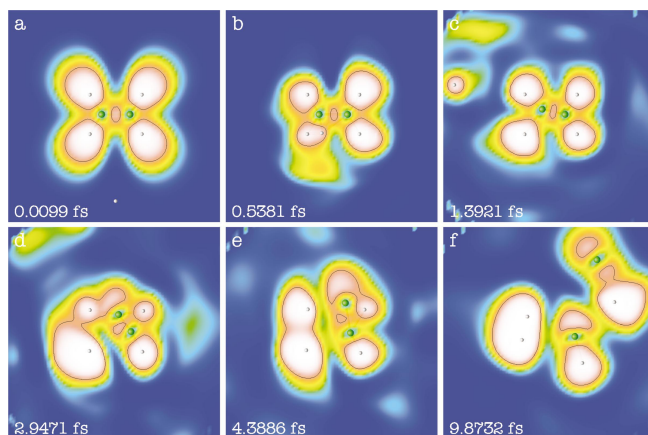
Fig. 3. Snapshots of the time-dependent electron localization (TD-ELF) for the scattering of a proton of energy $E_{kin} \simeq 2$ keV by an ethene molecule (C_2H_4, reproducing Fig. 2 of Ref. [32]). Same color scheme as in Fig. 2. The sequence shows the breaking of bonds and subsequent creation of lone pairs, leading to the fragmentation of the molecule into several pieces (H_2 and two CH). The full movie can be watched at [35].

nuclei under the effect of an external perturbation. In the next chapter, we present an example of a TRXRD study on the photodissociation of the I_3^- ion following excitation by light pulses of different wavelengths. *Ab initio* static DFT calculated data are already used to make an energetic balance of each possible reaction pathway from the reactant to the different possible solute species and to intepret TRXRD data. A more complete study of the full dynamics of the I_3^- photodissociation by TDDFT can be done in a way similar to the examples we have presented on acetylene under laser excitation and on the dynamics of ethene dissociation. This is already possible at the today computing power, although care is required when dealing with atomic elements well beyond the first rows of the periodic table.

Full TDDFT dynamics of the reaction paths in more complex molecules, like the photoactive yellow protein (PYP) also presented in the next chapter, are still out of reach. However, first TDDFT studies restricted only to the active regions of a protein, like chromophores into photoactive proteins, and to its electronic degrees of freedom were already possible, for example, on the green fluorescent protein (GFP) and its blue mutant (BFP) [36]. Although without a full ionic and electronic dynamics, we can supplement TRXRD studies by sampling a reaction path with electronic-only TDDFT calculations of excitations [36]. Along this line, one serious drawback is represented by the noncorrect representation of the so-called *conical intersections* (CIs) [37, 38] between potential energy surfaces of the ground and excited states (see Fig. 4). CIs play a fundamental role in photochemistry as the critical points that allow a given chemical reaction path from the reactants to
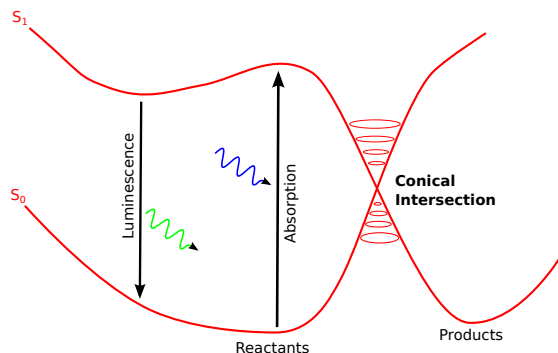
Fig. 4. Conical intersection (CI) between ground and excited states potential energy surfaces, allowing a radiationless decay in a photochemistry reaction.

the products. The identification of CI is already an important step forward in the study of photochemical reactions. Unfortunately, CIs are points where the traditional Born–Oppenheimer approximation breakdowns, and coupling between ionic and electronic degrees of freedom must be explicitly taken into account [39]. This is an active domain of research with many efforts also in the direction of evaluating the crossed validity of exchange-correlation and/or the Tamm–Dancoff approximations for a correct description of CI.

The examples presented in this section can give an idea of what TDDFT is going to achieve in the nearest future with increasing computer power and improved code algorithms, both in the direction of more involved studies and more complex systems. Indeed, with respect to other many-body approaches, TDDFT keeps at a reasonable computational cost and scaling ($O(N^4)$) with N the number of atoms in the molecule or periodic solid elementary cell), whereas TDDFT reliability is directly related to the limits of validity of the chosen approximation. For instance, TDLDA is expected to overestimate ionization rates due to its incorrect long-range behavior. Most of the present theoretical work go in the direction of improving standard approximations to correct this and other known drawbacks, like the mentioned problem of conical intersections.

11 TDDFT on EELS: local-field effects

We will now show examples of typical TDDFT results using the RPA and TDLDA approximations on electron energy-loss spectra (EELS) of a prototypical system like bulk silicon. Fig. 5 shows the EELS experimental spectrum measured [40] at $q \sim 0$, that is, almost zero-momentum transfer (red dots). The spectrum presents a single
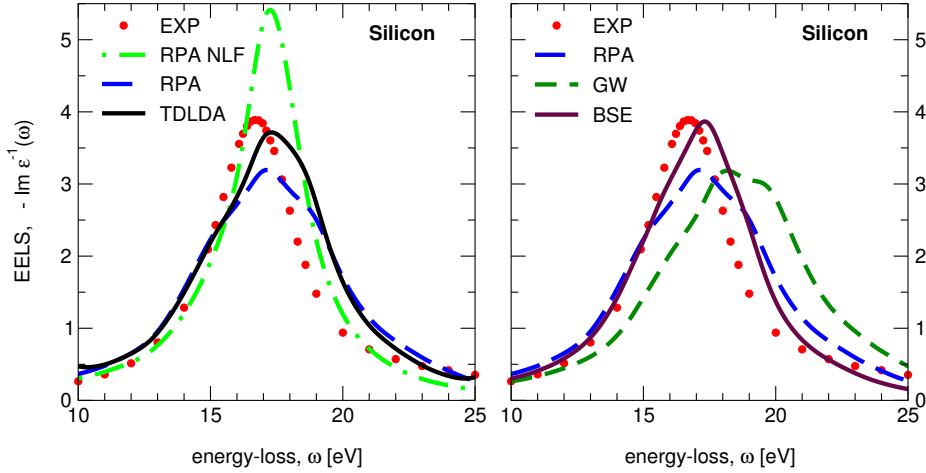
Fig. 5. Energy-loss spectra (EELS) in silicon at $q \simeq 0$ momentum transfer. Left (reproducing Fig. 3 of Ref. [42]): Energy-loss function in the RPA without (NLF, light green dot-dashed line) and with local-field effects (blue dashed line), TDLDA (black continuous line), EELS experiment (red dots from Ref. [40]). Right (reproducing Fig. 2 of Ref. [43]): Energy-loss function in the RPA (blue dashed line), GW-RPA (green dashed line), Bethe–Salpeter approach (BSE brown continuous line), EELS experiment (red dots from Ref. [40]).

peak at 16.7 eV, corresponding to the plasmon resonance collective excitation of bulk silicon. We then show the energy-loss function calculated [41] by the DP code in the RPA NLF (without local-field effects), the RPA (with local-field effects), and TDLDA approximations. We remark an overall agreement of TDLDA with the experiment. Both the position and strength of the plasmon resonance are correctly reproduced by the TDLDA approximation. We can also conclude that in this $q \sim 0$ case, the RPA result is not that bad and at least qualitatively in agreement. The plasmon energy is already well reproduced at the level of the RPA without local-field effects. Local-field effects improve on the resonance height.

This surprising result can be explained when looking at Fig. 5 (right panel), where we present the bulk silicon EELS calculated [43] by solving the Bethe–Salpeter equation (BSE) in the GW approximation within the framework of *ab initio* many-body quantum field theory. The latter is an approach relying on second quantization of fields and the electronic propagator or Green function $G(x_1, x_2)$ as fundamental degree of freedom, instead of the (time-dependent) density $\rho(x)$ of DFT and TDDFT. *Ab initio* many-body Green function theory is an alternative to DFT and TDDFT, with the important advantage that approximations within the theory are more easily to find by physical intuition. For example, the GW approximation to the self-energy can be seen as an evolution of the Hartree–Fock method by replacing the bare Fock exchange with a screened exchange, thus introducing some correlations in the form

of screening. The disadvantage of two-point Green functions $G(x_1, x_2)$ is that they are much heavier to calculate with respect to single-point densities $\rho(x)$ as in DFT and TDDFT. The scaling of Green function methods with the number of electrons is more unfavorable than in DFT and TDDFT, so that GW and BSE calculations are restricted to much simpler systems. Bulk silicon is still an affordable system for Green function methods, so that the GW and BSE results here can represent not only a comparison term for TDDFT, but also an invaluable tool to understand the physics at bench thanks to their more intuitive physical meaning. For instance, the GW approximation on the self-energy introduces electron–electron (e–e) interaction self-energy effects on top of the RPA approximation. In Fig. 5 we remark that the introduction of these effects (GW-RPA curve) surprisingly worsens the result. GW shifts the plasmon position to the highest energies and faraway from the experiment. On the other hand, introduction of electron–hole (e–h) interaction effects on top of GW, as by resolution of the Bethe–Salpeter equation (BSE curve), restores a good agreement with the experiment by shifting back again the plasmon resonance. To a large extent, e–e and e–h interaction effects compensate each other in EELS. As a consequence, the RPA lowest level of approximation, which neglects both effects, is already a good approximation. To improve upon RPA, we cannot introduce only one of them and should take into account both. This seems to be the case of the ALDA kernel, at least for EELS spectra.

We now discuss local-field effects and their importance. As introduced in Section 7, local-field effects are directly related to density inhomogeneities of the system. They enter into play with the departure from homogeneity and become increasingly important with the increase of density inhomogeneity. To illustrate these points, we take the example of graphite [44, 45], which is a system of intermediate 3D/2D character: it is in fact a 3D bulk solid, but its carbon atoms are arranged in 2D flat planes of graphene, weakly bounded and stacked one on top of the other. As a consequence of this particular atomic structure, the system looks homogeneous in the xy-direction, whereas it appears to be inhomogeneous along the z-direction. This can be appreciated in EELS by varying the direction of the momentum q transferred to the sample with respect to the system crystal axes. In Fig. 6 we report EELS spectra taken [44, 45] for graphite at almost zero-momentum transfer, $q \simeq 0$, but oriented along several directions: from the in-plane direction (q parallel to the graphene planes) to the out-of-plane direction (q perpendicular to the graphene planes and parallel to the z axis). The red dots are the spectra measured at the indicated experimental setup angles θ with respect to the z axis. We then report RPA spectra calculated with and without local-field effects (respectively LF and NLF). For momentum transfer in the in-plane direction, where EELS samples a homogeneous system, we cannot notice any appreciable difference between the RPA-NLF and RPA-LF spectra. Along this direction, local-field effects are negligible, and the RPA-NLF is a good approximation. Differences between spectra start to appear for q departing from the in-plane direction. Local-field effects become more and more
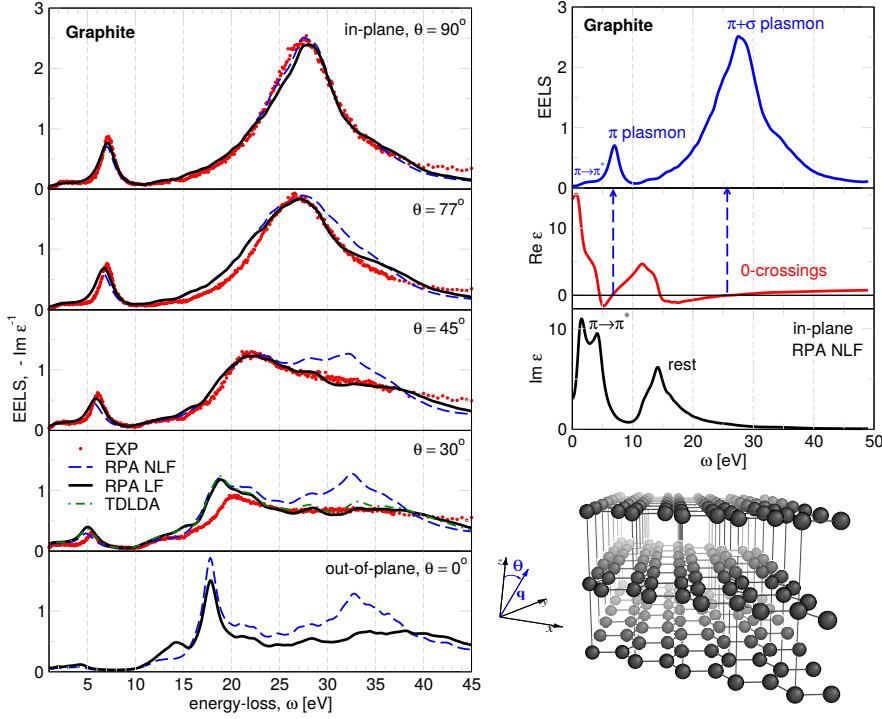
Fig. 6. EELS spectra of graphite (from Ref. [44, 45]) for small q transferred momentum at several directions, from in plane (top) to out-of-plane (bottom). Red dots: experiment; blue dashed line: RPA without LF effects; black solid line: RPA with LF; green dot-dashed line: TDLDA.

important by going toward the out-of-plane direction. Inclusion of them neatly improves the result: the RPA-LF result is in very good, quantitative agreement with the experiment at all sampled directions. Only the $\theta = 30°$ direction shows a small difference between the RPA-LF curve and the experiment, which is probably due to a small difference between the calculated and experimental angle of collection [44]. For this direction we also show the TDLDA spectrum which does not show any appreciable difference with respect to RPA-LF. Exchange-correlation effects, as accounted by the ALDA approximation, are small also in all other directions at almost zero, $q \simeq 0$, transferred momentum. Graphite is a good example to show the importance of local-field effects and their relation to density inhomogeneities.

Graphite is also a good example to show the fundamental contribution of *ab initio* theory to a correct interpretation of experimental findings. In Fig. 6, right, we report the in-plane RPA NLF graphite EELS spectrum, which we have already seen to be in quantitative agreement with the experiment. We also show in comparison the RPA NLF real ($\Re\varepsilon$) and imaginary ($\Im\varepsilon$) parts of the macroscopic dielectric function.

This comparison allows us to provide an unambiguous interpretation of EELS spectra and excitations. EELS peaks can be associated with either single-particle or collective excitations. Single-particle excitations are associated with electron–hole "optical" transitions, for example, the excitation of one electron from a valence to a conduction band as by a photon. They appear as peaks in the imaginary part of the dielectric function, which is directly related to the optical absorption (Section 7). EELS peaks that have a direct correspondence in the imaginary part of the dielectric function are to be classified as single-particle excitations. On the other hand, collective excitations are associated with the collective motion of the plasma of electrons, *e.g.* plasmons. A plasmon resonance is by definition in direct correspondence to the zeros of the real part of the dielectric function: indeed, at the frequencies where $\varepsilon(\omega) = 0$, the system supports self-sustained modes $E(\omega) = D(\omega)/\varepsilon(\omega)$ without the presence of an external field D. In graphite (Fig. 6, right), the only visible structure in the EELS that can be associated with a single-particle excitation is the low-energy shoulder from 0 to 6 eV, directly corresponding to the main peak in $\Im\varepsilon$, which is due to transitions from π to π^* states. The two main EELS peaks at 7 and 28 eV are both associated with zeros of $\Re\varepsilon$: therefore they are both bulk plasmon collective excitations. We can go further with the interpretation. The real and imaginary parts of the dielectric function are related by Kramers–Kronig relations, so that a peak in the imaginary part is followed by a characteristic s-shaped feature in the real part, occasionally producing a crossing to zero. In graphite the imaginary part presents two main absorption peaks: a low-energy peak (0–6 eV) due to single-particle excitations involving only transitions from π to π^* states, the closest to the Fermi energy, and a highest energy peak (14 eV), involving transitions also from σ and to σ^* states. This can be verified in an *ab initio* calculation (not in an experiment) by selectively removing those states from the calculation. In between the two main peaks the optical absorption falls almost to zero, so that also in the real part there is a separation between the two characteristic Kramers–Kronig features and the zero-crossings. The plasmon arising from the first low-energy 0-crossing is to be associated with the collective motion of only π electrons, whereas it is the collective motion of all (valence) electrons that gives rise to the highest energy plasmon. This justifies the interpretation of the two main graphite excitations as π-plasmon and total plasmon, respectively.

We conclude this section by discussing local-field effects under reduction of the system dimensionality, from 3D graphite to 2D graphene. In Fig. 7 we show the energy-loss function of graphene for the in-plane and the out-of-plane momentum transfer directions in the RPA with and without local-field effects. Like in graphite, local-field effects are negligible in the in-plane direction, where the electron density is homogeneous. On the other hand, local-fields are responsible for a strong suppression, a depolarization effect in the out-of-plane z direction along which the density goes to zero in the vacuum. The same effect can also be observed in 1D nanotubes or nanowires [47, 48] along directions orthogonal to the tube/wire axis. In Fig. 7, left,
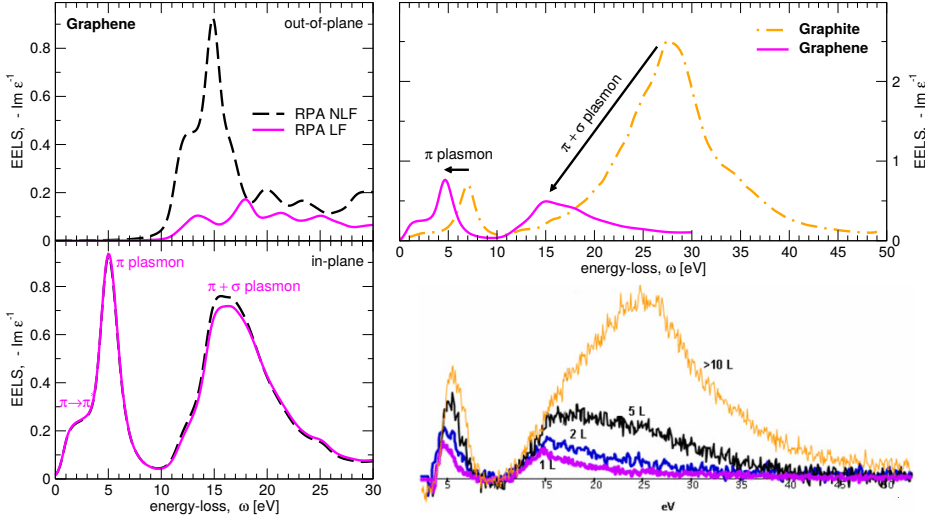
Fig. 7. Graphene vs graphite electron energy-loss spectra (EELS). Left: TDDFT RPA approximation calculation of graphene energy-loss function at $q \simeq 0$ for both out-of-plane (top) and in-plane (bottom) momentum transfer directions, with (magenta continuous lines) and without (dashed black lines) local-field effects. Right: TDDFT RPA LF energy-loss functions (top) of graphite (yellow dot-dashed line) and graphene (magenta continuous line) as compared to the EELS experiment by Eberlein et al. [46] (bottom) for a single graphene monolayer (pink curve), two layers of graphene (blue), five (black) and more than ten layers of graphene (yellow).

we show the in-plane EELS spectra calculated by TDDFT in the RPA LF approximation for both graphite and graphene. In the same figure, right, we also show the experimental [46] EELS spectra taken for one graphene monolayer, and up to ten layers of graphene that, from a dielectric point of view, can already be considered bulk graphite. The TDDFT calculation [49, 50] predicted the correct shift of both plasmons in going from graphite to graphene (shifts emphasized by the black arrows in the top-right panel of Fig. 7), although with an overestimation of the oscillator strength of the π plasmon.

12 TDDFT on IXSS: exchange-correlation effects

We have seen that in EELS spectra at almost zero-momentum transfer, $q \simeq 0$, exchange-correlation effects as accounted by the adiabatic LDA approximation are small, and the RPA approximation is already in a very good agreement with the experiment. This is not the case for finite momentum transfer. Exchange-correlation effects become more important when going to the largest q. Although it is possible to acquire energy-loss spectra at small though finite q, an experimental technique that
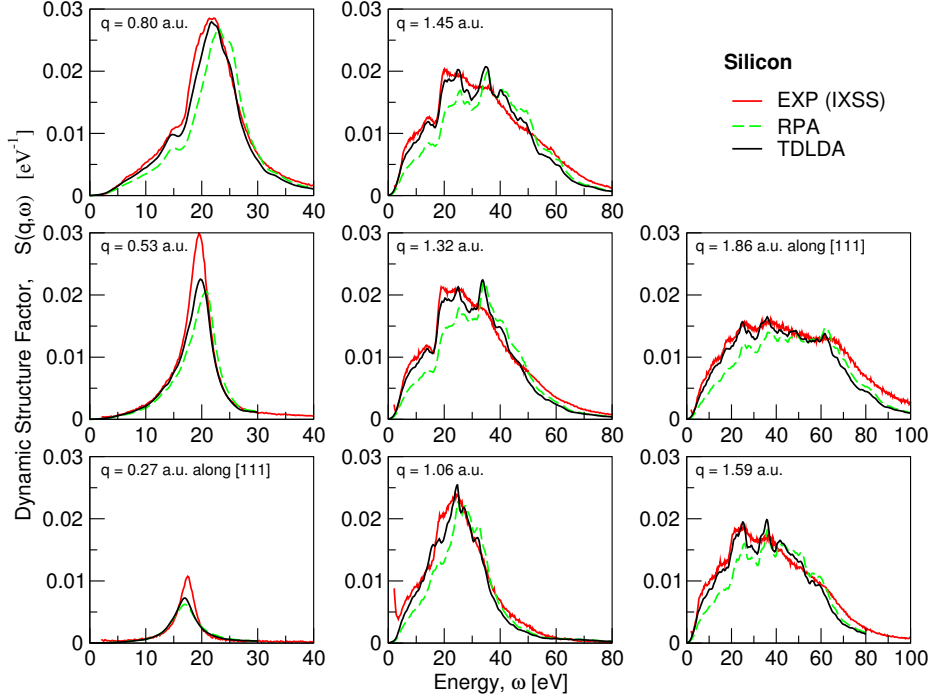
Fig. 8. Silicon dynamic structure factor $S(q, \omega)$ for different transferred momenta q along the [111] direction (from Ref. [51]). Red lines: experimental inelastic X-ray spectrum (IXSS) taken at the European synchrotron radiation facility (ESRF); green dashed lines: TDDFT in the RPA with local-field effects approximation; black lines: TDDFT in the ALDA approximation.

allows us to access the range of very large q (up to several Brillouin zones) is inelastic X-ray scattering spectroscopy (IXSS). IXSS requires to use intense synchrotron radiation X-rays as primary beam and detects the scattered photons at given angle related to the momentum transfer. IXSS measures the dynamic structure factor $S(q, \omega)$, which is related to the macroscopic dielectric function $\varepsilon_M(q, \omega)$ by

$$S(q, \omega) = \frac{q^2}{4\pi^2 \rho} \left(-\Im \varepsilon_M^{-1}(q, \omega) \right),$$

where ρ is the electron density. We see that the dynamic structure factor is directly proportional to the energy-loss function $-\Im \varepsilon_M^{-1}$, so that EELS and IXSS measure in practice the same observable, though with different resolution at different regimes.

Again for the prototypical bulk silicon, we show in Fig. 8 the experimental dynamic structure factor [51] at different transferred momenta along the [111] direction. Once again, we compare the experiment to the TDDFT results in the RPA with local-field (LF) effects and the TDLDA approximations. At the smallest q the two approximations provide almost no different results, like we have already seen
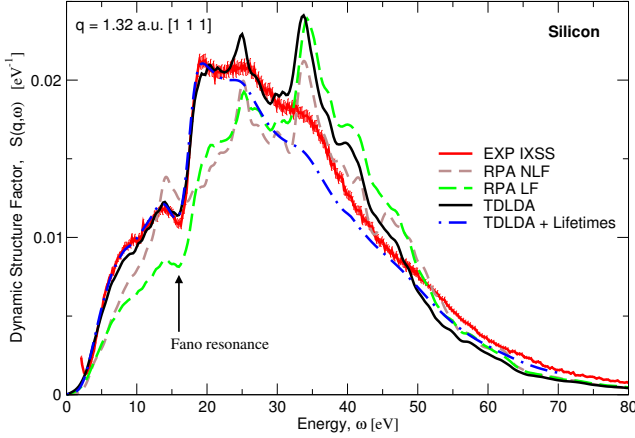
Fig. 9. Silicon dynamic structure factor at $q = 1.32$ a.u. along the [111] direction (from Fig. 4 of Ref. [42] and Fig. 1 of Ref. [51]). Red line: IXSS experiment [52, 51]; short-dashed brown line: TDDFT in the RPA without local-field effects (NLF) approximation; long-dashed green line: TDDFT in the RPA with local-field (LF) effects; black continuous line: TDDFT in the ALDA approximation (TDLDA); blue dot-dashed line: TDLDA plus lifetime effects.

for $q \simeq 0$ at the example of graphite (Fig. 6). Exchange and correlation effects, as accounted by the adiabatic LDA exchange-correlation kernel, are negligible at the lowest q but become more important with increasing q. At $q = 0.80$ a.u., we observe an already marked difference of TDLDA with respect to RPA in the direction of an improved agreement with the experiment. At the largest q, TDLDA and RPA present large differences, especially in the low-energy spectral range where TDLDA is in an almost quantitative agreement with the experiment. Two conclusions can be drawn: 1) in the energy-loss function, exchange and correlation effects are important at the largest transferred momenta; 2) adiabatic LDA is a good approximation to the TDDFT exchange-correlation kernel at least on the energy-loss function low-energy range.

In Fig. 9 we focus on the $q = 1.32$ a.u. to provide an analysis with more details. The effect of local fields can be appreciated as nonnegligible by comparing RPA LF and NLF spectra. Local-fields have the effect to push spectral weight from low to high energies. Surprisingly, the RPA NLF result appears closest to the experiment. Inclusion of exchange-correlation effects on top restores a good result, as if there were a compensation between LF and xc effects. However, a more careful analysis shows that the RPA NLF result cannot even qualitatively capture important aspects. At 17 eV the experiment presents a characteristic asymmetric feature (small peak/shoulder followed by a steep rise) typical for a Fano resonance [53]. This is the interpretation given by Schülke *et al.* [54] by using a model. The Fano resonance would result from the interaction of the silicon plasmon ~ 17 eV discrete excitation (see the $q \simeq 0$ EELS

in Fig. 5) with the continuum of electron–hole excitations. In Fig. 9 we can see that TDLDA is in a quantitative agreement with the experiment in the low-energy range and up to 22 eV. The 17 eV asymmetric feature is perfectly reproduced by TDLDA. This is also the case for the RPA LF result, apart from an underestimation of the spectral intensity. On the other hand, we observe a peak at 17 eV in the RPA NLF result, but we do not observe the characteristic asymmetry with the following steep rise. We can see that local-fields, related to nondiagonal elements of the microscopic dielectric matrix, play an important role in the Fano mechanism.

Finally, we observe that the TDLDA result starts to present deviations from the experiment beyond 22 eV. We observe well-defined peaks, which are however in correspondence to perceptible structures in the experiment. This disagreement has been attributed to lifetime effects [51] that in principle are accounted by the exact exchange-correlation kernel f_{xc} of TDDFT but not by the TDLDA approximation. An approximative inclusion of such effects, as by introducing a Fermi-liquid imaginary part to the single-particle energies or by adding an equivalent non-Hermitian kernel f_{xc}^{LF} [51], would produce a better result like the TDLDA + Lifetime spectrum of Fig. 9. From the present example we can conclude that the adiabatic LDA approximation can already bring an important part of exchange-correlation effects but of course presents its limits. One of them is certainly the lack of lifetime effects.

We can think that the very good performances of TDDFT on the energy-loss function and related observables we have shown so far are restricted only to particularly simple systems, like silicon, graphite and graphene. We may wonder about the limits and a breakdown of TDDFT on a more complex system, like, for example, strongly-correlated systems. In reality, TDDFT is in principle an exact theory to calculate *neutral* excitation and optical/energy-loss spectra. This is granted by the Runge–Gross theorem and all the formal developments of the theory. So exact, nonapproximated TDDFT is able to describe energy-loss spectra no matter the condensed matter system. However, we might ask about the limits of the adiabatic LDA approximation and a breakdown of TDLDA on more complex systems. High-temperature superconductors cuprates can certainly be considered a severe workbench to check the validity of TDLDA. The cuprate pairing mechanism allowing such high critical temperatures is so far unknown, albeit 30 years of theoretical efforts. A large part of the scientific community believes that the pairing mechanism and superconductivity are related to a strong correlation physics. They certainly show nonconventional, not yet explained physics. Checking the validity of TDLDA on the energy-loss function of cuprates can represent a severe workbench for the ALDA approximation. The energy-loss function is in particular related to the screening of the system and so also to antiscreening ranges where the the pairing is going to occur. So, study of the energy-loss function and of the screening is not even a marginal one for the purpose of understanding superconductivity mechanisms.

In Fig. 10, we report the dynamic structure factor $S(q, \omega)$ of YBCO ($YBa_2Cu_3O_7$) as a function of exchanged energy and momentum [55]. The experimental $S(q, \omega)$
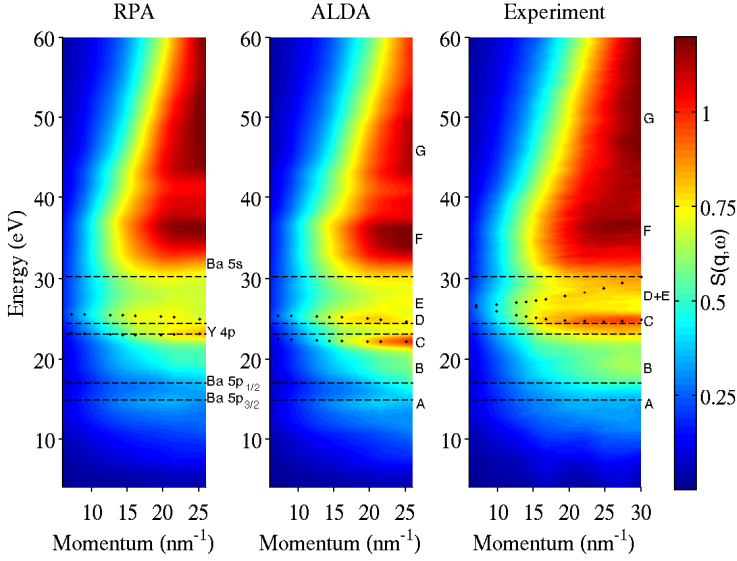
Fig. 10. Inelastic X-ray scattering spectra (IXSS) in YBCO (Ref. [51]). The dynamic structure factor $S(q, \omega)$ is plot in false colors (rightmost bar) as a function of exchanged momentum and energy. The first two panels refer to TDDFT calculations of $S(q, \omega)$ in the RPA (with local field effects) and ALDA (TDLDA) approximations, whereas the third is the IXSS experiment taken at the European synchrotron radiation facility (ESRF). The most prominent spectral features are labeled A-G on the ALDA and experimental plots. The nominal core-electron excitation energies are marked with dashed lines and labeled in the RPA plot. The dispersion of features C and D are marked with dots as a guide for the eye.

has been measured by an IXSS experiment at the European Synchrotron Radiation Facility (ESRF) on a YBCO sample in the normal phase. The theoretical spectra are TDDFT calculations in the RPA with local field effects and ALDA (TDLDA) approximations. Already at a first look, the complexity and the physical richness of this system are immediately evident. We cannot enter into the detailed interpretation of all the excitations in YBCO, like we did for graphite, and their effect on the dielectric screening. This can be found in the original reference [55]. Here we just only report that even in YBCO the TDLDA approximation does not breakdown and is perfectly able to describe and interpret almost all excitations together with their dispersion in the experimental dynamic structure factor (apart from the energy region D+E in the figure, for which a discussion is provided in [55]). Although the spectra reported here and in Ref. [55] refer to the normal, nonsuperconducting phase of YBCO, it can nevertheless be considered a success of TDDFT. Manifestations of a nonconventional physics are indeed already present in the normal phase, and the whole phase diagram of cuprates still awaits for a coherent explanation.
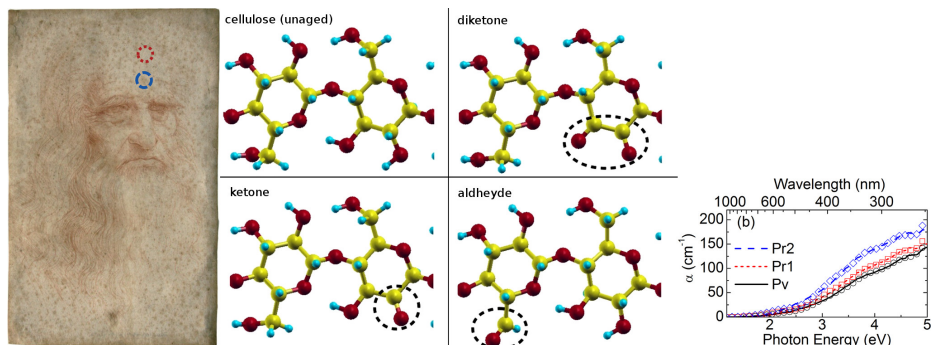
Fig. 11. Experimental (lines) and TDDFT theoretical (symbols) optical absorption spectra (right) of three spots on Leonardo Da Vinci's iconic self-portrait (left, Pr2 in blue, Pr1 in red, Pv in black and taken on the back side of the portrait). The atomic structure of pristine cellulose and three representative oxidized groups (evidenced by dashed circles) of aged cellulose, diketone, ketone, and aldhehyde, is shown in the middle panel. (Reproducing Fig. 1, 2, and 3 of Ref. [56]).

13 Optical spectroscopy: TDLDA drawbacks

We begin this section by presenting an example of application to the study of optical properties where TDDFT and theory brought an important contribution: the study of the optical visual degradation of Leonardo Da Vinci's iconic self-portrait (Fig. 11, [56, 57]). Diagnostic studies of the state of conservation and degradation causes and rates of artworks are an invaluable information for conservators and restorers to establish the best conditions for their public enjoy, if suitable, or to plan possible restorations. Access to the most precious or most degraded artistic heritage by intrusive and destructive experimental techniques is very often refused by art critics and operators. This was the case of the Leonardo Da Vinci's self-potrait, red chalk on paper, nowadays not anymore exposed to public and external agents. For a diagnostic study of its conservation state, the acquisition of optical spectra by only reflection under exposure to ordinary (nonintense and noncoherent) light were solely agreed. Without the possibility of an ordinary chemical analysis of a small piece of the artwork or other experimental manipulations, resort to theory was the only possibility to characterize the state of degradation of the masterpiece.

TDDFT optical spectra calculations by the DP code were carried out for pristine cellulose, main component of paper, and several products of cellulose ageing, oxidized groups such as diketone, ketone, and aldhehyde (some of them shown in Fig. 11) that act as chromophores and are responsible for the yellowing of cellulose. Theoretical TDDFT spectra were calculated and then used as a reference to characterize experimental spectra measured at different spots on the artwork, chosen to

explore the largest range of its conservation state, from the best conserved to the most degraded points (indicated on the portrait in Fig. 11). A linear combination of TDDFT spectra corresponding to single oxidized groups was determined by a best fit with the experimental spectra. The linear coefficients of the fit provided an estimate of the concentration of chromophores responsible for paper ageing and made it possible to obtain chemical information of the artwork by nondestructive and nonintrusive optical measures. This has allowed us to establish the present status of the masterpiece — to be compared with future analysis for a measure of the degradation rate — and the main causes of degradation along the artwork history, *e.g.*, moisture, to be carefully avoided in any future conservation program.

The very good match between TDDFT and measured spectra in Fig. 11 is effective, *i.e.*, we cannot obtain it by simply adjusting the fitting coefficients in a linear combination of spectra of other chromophores or completely different materials that are certainly absent from the artwork [56, 57]. We can be surprised by the accuracy of TDDFT calculations that were carried out using the adiabatic local-density approximation (ALDA or TDLDA). As we will illustrate in the following, TDLDA present severe drawbacks on optical spectra of infinite bulk solids, like, for example, an underestimation of the optical absorption onset. For instance, the TDLDA gap of bulk cellulose was found to be 5.15 eV, whereas cellulose does not absorb light above 200 nm (below 6 eV). However, the yellow color seen in aged paper is mainly due to oxidized cellulose chromophores, absorbing below 5 eV and in the highest energy band of visible light, violet and blue, and continuing to scatter lowest energy yellow and red photons. These absorption peaks are due to transitions between electronic states that are localized around the oxidized groups, in practice to be considered as defects of the cellulose bulk crystal. So, the orbitals involved in this range of the optical spectrum and in these transitions are very much localized on the chromophore defects and do not mix with delocalized periodic Bloch states. A local exchange-correlation approximation can be expected to work reasonably well in these situations, and this explains the good results obtained by Refs. [56, 57]. So, on optical spectra of defects, like also in isolated systems as atoms or molecules, TDLDA works reasonably well and much better than in periodic solids, as we will see in the next example.

TDDFT is an in principle exact theory to calculate all neutral excitations and so also optical spectra. The question is whether the most common TDDFT approximations RPA and TDLDA are good enough to capture the physics of excitations of, *e.g.*, optical absorption. Fig. 12 presents the experimental imaginary part of the macroscopic dielectric function $\Im\varepsilon(\omega)$ (red dots), directly related to the optical absorption, measured by the ellipsometry experiment of Ref. [58] in bulk silicon. In the same figure, we show TDDFT calculations, as by the DP code [41], of the RPA with and without LF effects and TDLDA spectra. We remark "some" qualitative agreement of TDDFT with the experiment: we observe in the experiment three peaks, at 3.5, 4.3, and 5.3 eV, which are more or less reproduced by three structures in
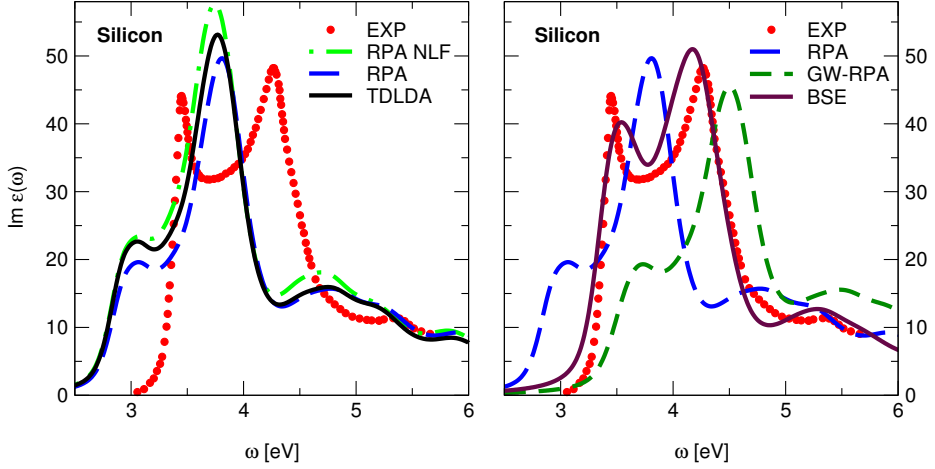
Fig. 12. Optical absorption in silicon. Left (reproducing Fig. 2 of Ref. [42]): Imaginary part of the macroscopic dielectric function in the RPA without (NLF, green dot-dashed line) and with local-field effects (blue dashed line), TDLDA (black continuous line), ellipsometry experiment (red dots from Ref. [58]). Right (reproducing Fig. 1 of Ref. [59]: Imaginary part of the macroscopic dielectric function in the RPA (blue dashed line), GW-RPA (green dot-dashed line), Bethe–Salpeter equation approach (BSE, brown continuous line), ellipsometry experiment (red dots from Ref. [58]).

the theory, whether in the RPA or TDLDA approximation. Comparing RPA curves with LF and without it (NLF), local-field effects seem to have the same weight as exchange-correlation effects. We also remark that there is no improvement in going from the RPA to the TDLDA approximation. The agreement with the experiment is unsatisfactory for two reasons:

1. The TDLDA (or RPA) optical onset appears red-shifted by ~ 0.6 eV with respect to the experiment. Not only the onset, but also the whole spectrum seems rigidly red-shifted with respect to the experiment by those 0.6 eV.
2. The height of the first lowest energy peak seems underestimated by the theory with respect to the experiment. Both in RPA and TDLDA, this peak appears like a shoulder of the main peak, whereas in the experiment, it is of almost the same height. Nevertheless, we remark some agreement between theory and experiment on the height of the second and third highest energy peaks.

The cause of the first problem seems quite easy to trace. Indeed, 0.6 eV is exactly the band gap underestimation of the DFT-LDA Kohn–Sham electronic structure with respect to the true, quasiparticle electronic structure in silicon. A quasiparticle self-energy calculation, as in the GW approximation [60, 61] within the framework of many-body perturbation theory, takes into account in a satisfactory way correlation

electron–electron (e–e) interaction effects and corrects the DFT band gap underestimation. A GW-RPA spectrum, calculated using an RPA approximation on top of a GW electronic structure, appears blue-shifted with respect to the KS-RPA spectrum by a 0.6 eV (see the GW-RPA curve in Fig. 12, right). GW-RPA improves on the position of the optical onset and all other structures. The remaining discrepancies with the experiment, in particular the underestimation of the first low-energy peak, have to be ascribed to electron–hole (e–h) interaction effects still missing in the GW-RPA approximation to the polarizability. Inclusion of e–h interaction diagrams to the polarizability (vertex corrections), as by solution of the Bethe–Salpeter equation (BSE) within the framework of many-body perturbation theory, fully captures all the physics involved in optical spectroscopy. This is demonstrated by a BSE calculation [59] of the silicon optical absorption. The BSE curve (Fig. 12, right) corrects the underestimation of the first peak and is in a good agreement with the experiment.

Apparently, BSE seems also to slightly blue-shift the GW-RPA spectrum. However, accurate verification of results [59] has shown that in silicon there is negligible (< 0.1 eV) BSE correction to GW excitation energies. The first absorption peak in silicon is not really a bound exciton, *i.e.*, an electron–hole bound state. Nevertheless, its strength is strongly determined by electron–hole interaction (excitonic) effects. So the reshape of the spectrum from GW-RPA (without e–h) to BSE (with e–h interaction effect) is just only a redistribution of oscillator strength from high to low energies. This transfer of oscillator strength from high to low energy is the typical e–h interaction *excitonic effect* in small band-gap semiconductors. In these systems the screening is intermediate between metals and insulators.

The effect of e–h interactions is much more spectacular in large band-gap insulators, where interactions are almost unscreened. An electron promoted by a photon into a conduction state interacts strongly with the hole left in the valence band, so that they can be bound into an *exciton* at an energy level lower than a pair of free electron and hole. In the optical absorption spectrum, excitons appear as discrete peaks at an energy lower than the band-gap which corresponds to the onset of the continuum of electron–hole pairs. This is particularly evident in solids of rare gas elements.

In Fig. 13, we report the experimental [63] optical absorption spectrum (red dots) of solid argon. The band-gap in solid argon is 14.2 eV, and the dielectric constant is very close to 1. At a low energy, we observe discrete peaks, which are available optical excitations of the system within the band-gap: this is a whole series of bound excitons due to e–h interaction effects. The energy difference between the band-gap/onset of the continuum and the exciton is defined as the *exciton binding energy*. In solid argon the binding energy of the first exciton is up to 2 eV, among the largest exciton binding energies. In Fig. 13, we present also TDDFT spectra. Both the RPA and the TDLDA approximations miss completely the excitons and produce an unsatisfactory result, unlike silicon far to be even qualitative. Within many-body perturbation theory the GW-RPA approximation corrects the onset of
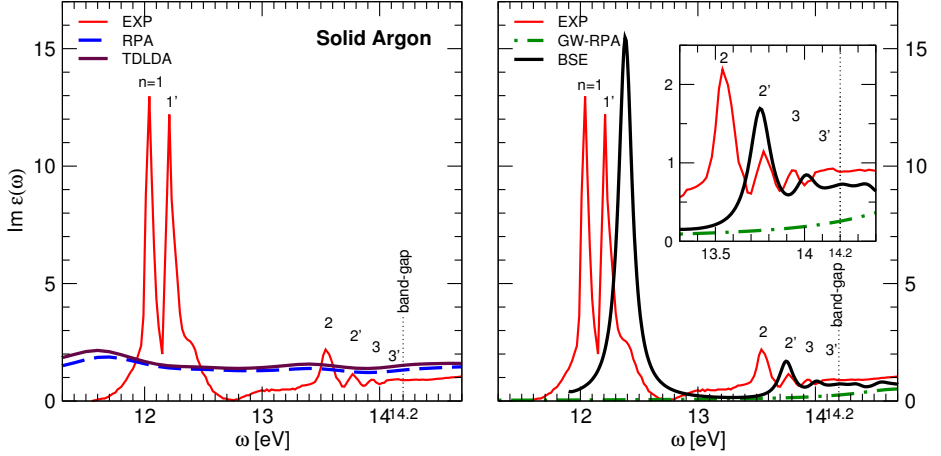
Fig. 13. Optical absorption in solid argon (from Ref. [62]). Left: red line, experiment; blue dashed line, RPA; brown continuous line, TDLDA. Right: red line, experiment; dot-dashed green line, GW-RPA; black continuous line, Bethe–Salpeter equation result. There are two exciton series, the spin triplet n and the singlet n'. Nonspin-polarized calculations are supposed to reproduce only the spin singlet n' series. The band-gap is 14.2 eV in argon.

the continuum, aligning it to the band-gap energy, but still misses the excitons. Only the Bethe–Salpeter equation introduces the right physics to capture excitons. In the optical absorption of solid argon the BSE correction to GW-RPA is spectacular.

Within many-body perturbation theory, the Bethe–Salpeter equation on top of the GW approximation proved to contain the right many-body physics to describe optical properties of condensed matter systems. On the other hand, within TDDFT, the RPA and also the ALDA approximations do not contain such many-body physics. Note that this is a drawback of the approximations, not of TDDFT, which is in principle an exact theory for optical excitations. The problem is that the ALDA approximation is missing some important characteristics of the *exact* xc kernel directly related to e–h interaction effects.

14 Beyond TDLDA: long-range contribution (LRC) kernel and developments

Both in solid argon and in silicon (Fig. 12 and 13),we have seen that the TDLDA optical absorption is almost coincident with the RPA. A local kernel like ALDA has in practice no effect. This can be explained by the following argument [41]: the xc kernel appears in Eq. (19) only in a term $\chi^{\mathrm{KS}} f_{\mathrm{xc}}$, where it is coupled to the Kohn–

Sham polarizability χ^{KS}. In the optical limit as $q \to 0$, the Kohn–Sham polarizability goes to zero as $\lim_{q\to 0} \chi^{\mathrm{KS}}(q) \sim q^2 \to 0$, as it can be seen from Eq. (33) and from the fact that $\rho_{ij}^{\mathrm{KS}}(q) \sim q \to 0$. A local kernel like ALDA behaves as a constant as $q \to 0$, $\lim_{q\to 0} f_{\mathrm{xc}}^{\mathrm{ALDA}} = \mathrm{const}$, so that the term $\lim_{q\to 0} \chi^{\mathrm{KS}} f_{\mathrm{xc}}^{\mathrm{ALDA}} = 0$ goes to zero in the optical limit. This explains why ALDA results cannot differ from taking *tout court* $f_{\mathrm{xc}} = 0$, like in RPA. To depart from RPA, we have to consider xc kernels containing nonlocal contributions. First attempts having introduced semilocal or short-range nonlocality [42, 41] proved to be still not sufficient. The true exact kernel of insulators and semiconductors must contain an *ultra*nonlocal, long-range $1/q^2$ Coulomb-like contribution. In the optical limit an ultranonlocal kernel diverges, $\lim_{q\to 0} f_{\mathrm{xc}} = \infty$, in such a way to have a finite contribution from the $\chi^{\mathrm{KS}} f_{\mathrm{xc}}$ term. This is the only way for an xc kernel to produce in the optical limit a departure from the RPA $f_{\mathrm{xc}} = 0$ approximation [64].

A first step toward the solution of TDLDA drawbacks on optical excitations in semiconductors and insulators was the introduction of the so-called long-range contribution (LRC) only, also dubbed α/q^2 kernel for its mathematical shape in reciprocal space [41, 65],

$$f_{\mathrm{xc}}^{\mathrm{LRC}}(q) = \frac{\alpha}{q^2}. \tag{34}$$

Here α is a material-dependent parameter that should reduce to zero in metals and in jellium (homogeneous electron gas) model, which is known not to present an LRC contribution in its kernel. From the Fourier transform in real space,

$$f_{\mathrm{xc}}^{\mathrm{LRC}}(r, r') = \frac{\alpha}{4\pi|r - r'|}, \tag{35}$$

it can be seen that this kernel contains an ultranonlocal, *i.e.*, a long-range Coulomb-like contribution. This is an important difference with respect to the local ALDA kernel, Eq. (25), but also with respect to nonlocal or semilocal kernels [42]. As we will see, this is the characteristics that must be owned by the true exact xc kernel of insulators and semiconductors to properly account for *e–h* interaction and, more generally, many-body effects.

When introducing a kernel of the form α/q^2 [64], the optical absorption (TDDFT KS-LRC curve in Fig. 14) finally starts to differ appreciably from RPA and TDLDA. We observe a redistribution of spectral weight from low to large energies when taking a positive ($\alpha > 0$) LRC. At increasing α, the first peak is more and more damped, until we can achieve a situation where the optical onset arises at larger energies, thus correcting the Kohn–Sham band-gap underestimation. However, for a kernel of the simple only one-parameter form α/q^2, it is difficult to correct both RPA drawbacks, *i.e.*, the underestimation of the optical onset (lack of *e–e* interaction effects) and the underestimation of the low-energy spectral weight (lack of *e–h* excitonic effects). Of course, the true exact kernel should correct the Kohn–Sham independent particle polarizability χ^{KS} for *both* effects. In general the kernel can always be split into two
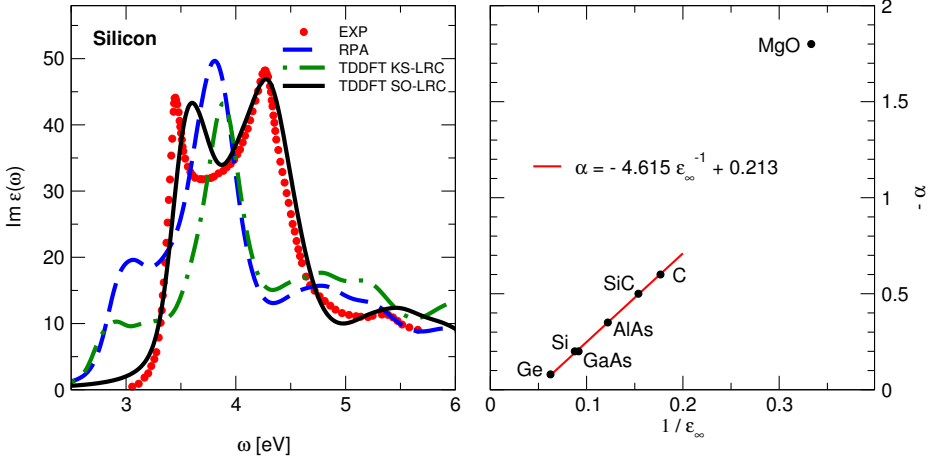
Fig. 14. Optical absorption in silicon. Imaginary part of the macroscopic dielectric function in the TDDFT RPA approximation (blue dashed line), LRC on top of χ^{KS} (green dot-dashed line, reproducing with higher convergence solid line of Fig. 6.5 in Ref. [41]), LRC on top of χ^{QP} (black continuous line, reproducing Fig. 1 of Ref. [65]), and ellipsometry experiment (red dots from Ref. [58]). Right: Relationship $|\alpha|$ parameter (y-axis) dielectric constant ε_∞^{-1} (x-axis) (reproducing Fig. 12 of Ref. [66]) for several materials.

components:

$$f_{\mathrm{xc}} = f_{\mathrm{xc}}^{e\text{-}e} + f_{\mathrm{xc}}^{e\text{-}h}. \tag{36}$$

The first component introduces e–e self-energy effects and brings the Kohn–Sham polarizability χ^{KS} to a quasiparticle GW-RPA polarizability χ^{QP},

$$\chi^{QP} = \chi^{KS} + \chi^{KS} f_{\mathrm{xc}}^{e\text{-}e} \chi^{QP}, \tag{37}$$

whereas the second term introduces e–h excitonic effects and leads to the final full polarizability χ,

$$\chi = \chi^{QP} + \chi^{QP}(w + f_{\mathrm{xc}}^{e\text{-}h})\chi. \tag{38}$$
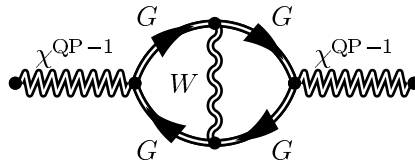
In practice [65], we can skip the first step and directly calculate χ^{QP} by an Adler-Wiser formula, Eq. (18), using a rigid *scissor operator* (SO) correction of Kohn–Sham conduction energies with respect to valence. The SO correction can be adjusted to the *ab initio* GW band-gap correction, which is in a good agreement with experimentally measured band-gaps. This should provide a result close to the GW-RPA spectrum of Fig. 12. The remaining task of introducing e–h excitonic effects is then taken by an $f_{\mathrm{xc}}^{e\text{-}h} = f_{\mathrm{xc}}^{\mathrm{LRC}} = \alpha/q^2$ long-range contribution kernel. This term has the task to transfer oscillator strength in the backward direction, from high to low energies, exactly like BSE on top of GW (see Fig. 12). This is done by a negative divergence, $\alpha < 0$.

The result of this TDDFT SO-LRC approach [65] is presented for silicon in Fig. 14. The TDDFT SO-LRC is in practice as good as the Bethe–Salpeter result with respect to the experiment, but at a much cheaper computational cost. The BSE and LRC kernels seem to reproduce the same physics, *i.e.*, the transfer of spectral weight from high to low energy, characteristic of excitonic effects in intermediate screening semiconductors. The amplitude of the transfer is modulated by the parameter α, and the direction is due to its negative sign. The strength α of the divergency should be inversely proportional to the screening in the system. The smaller the screening (large band-gap insulators), the larger α. α is expected to be 0 for metals (*e–h* interaction fully screened). In fact, it can be found that an α provided by the linear expression

$$\alpha = -4.615\varepsilon_\infty^{-1} + 0.213 \tag{39}$$

(see also Fig. 14), where ε_∞ is the dielectric constant of the material, either experimental or RPA (with some correction to the coefficients), can provide results close to the BSE approach and in a good agreement with the experiment. For silicon, we have $\alpha \simeq -0.2$.

This approximation provides a good result for semiconductors and small bandgap insulators like diamond, but it breaks down for large band-gap insulators (*e.g.*, MgO) and in particular in systems presenting more than one bound exciton. We can further complicate the LRC expression, introducing more than one parameter or a frequency dependence [67, 68] and have some improvement but at the cost of more and more empirical expressions. Following a less empirical route and by reverse engineering from the Bethe–Salpeter equation, we can derive an expression of the TDDFT xc kernel related to the BSE kernel $\Xi = W$, where $W = \varepsilon^{-1}w$ is the screened Coulomb interaction. This kernel, dubbed *Nanoquanta kernel* (NQ) [65, 69, 70, 71, 72, 73, 74, 75] can be written in a diagrammatic condensed form as

$$f_{xc} = \chi^{\text{QP}-1}GGWGG\chi^{\text{QP}-1} =$$

where G is the Green function, *i.e.*, the electron (forward) or the hole (backward arrow) propagator. This kernel is rooted into the Bethe–Salpeter kernel $\Xi = W$, which introduces the interaction between the electron and the hole (the wiggly line between the electron and hole propagators). When plugged into the TDDFT Eq. (19), the NQ kernel must provide by construction the same result as the Bethe–Salpeter equation.

The Nanoquanta kernel result [62] for solid argon is presented in Fig. 15. Like the Bethe–Salpeter kernel (Fig. 13), the NQ kernel is able to reproduce the complete series of three peaks associated with bound excitons in argon, whereas RPA, TDLDA,
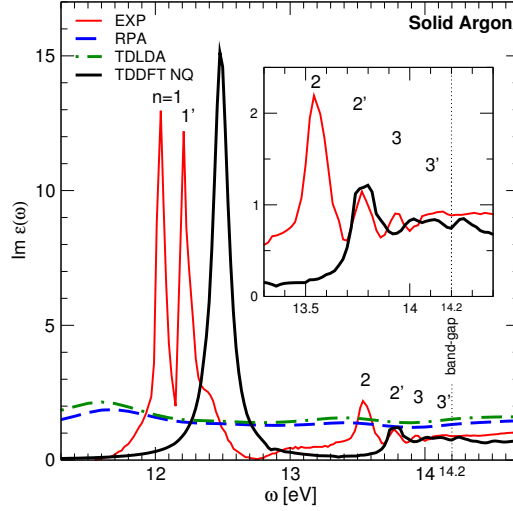
Fig. 15. Optical absorption in solid argon (from Ref. [62]). Red line: experiment; blue dashed line: RPA; green dot-dashed line: TDLDA; black continuous line: Nanoquanta (NQ) kernel. There are two exciton series, the spin triplet n and the singlet n'. Nonspin-polarized calculations are supposed to reproduce only the spin singlet n' series. The band-gap is 14.2 eV in argon.

and GW-RPA fail. Note that this Nanoquanta approach has addressed also the other xc kernel $f_{xc}^{e\text{-}e}$ term responsible for the e–e interaction self-energy effects. This has demonstrated that a full TDDFT kernel, able to account for both e–e and e–h, exists and can be calculated, though with a computational effort not much cheaper than the many-body GW and BSE approach.

More recent developments have tried to improve upon the Nanoquanta and LRC kernels by following self-consistent approaches [76], by relying on beyond LDA, *e.g.*, meta-GGA functionals [77, 78] within pure TDDFT, and finally, relying on approximations beyond LDA and not routed anymore into the jellium model, toward, *e.g.*, the jellium-with-gap model [79].

15 Outlook and conclusions

We have provided a simple but necessarily incomplete introduction to TDDFT, reviewing just only the main issues and some of the problems still awaiting for a solution. Among the main challenges still in front, we can mention: the description of the Rydberg series in atoms (Section 9); double excitations in molecules [80], where two electrons are promoted to excited states, which questions the validity of the adiabatic approximation; charge-transfer excitations in organic molecules, that is, excitations

where the electron and hole wavefunctions have small or no overlap; conical intersections in photochemistry reaction paths (Section 10), where the Born–Oppenheimer approximation is under question; memory effects in the electron and ion dynamics (Section 10); many-body effects in optical spectra of solids (Section 14). All these are problems of the approximations to the exchange-correlation functional, not of TDDFT theory itself. As illustrated at the example of optical spectra, developments beyond standard approximations (*e.g.*, adiabatic LDA, GGA, etc.) have the potentiality to cure or alleviate these problems. For more complete reviews of TDDFT problems, challenges, developments, and perspectives, we refer to Refs. [81, 82] and references therein.

We have provided only a few examples where the vast majority of TDDFT applications mainly lie, excitations and spectroscopy in the linear response regime, and where also standard approximations work better. We have also shown some examples of beyond-linear electron and even ion dynamics (Section 10), out of the few nonlinear TDDFT applications available in the literature. We would like to mention here very recent applications of TDDFT to nonlinear optics [83, 84], allowing the access to multiple photon excitations by intense lasers, second harmonic generation, and providing spectra in a good agreement with experiments. Next years experimental developments going in the direction to have more intense and coherent laser and X-ray sources (like the XFEL facility in Hamburg), with improved spatial resolution and with pump and probe setups allowing the study of the time evolution with a resolution achieving the femtosecond and below, will certainly stimulate TDDFT developments and applications in the same direction. The dynamics of the fragmentation of the ethene molecule (Section 10) is today an isolated but promising example of what TDDFT can do in the next years to supplement future experiments, understand mechanisms beyond physical, chemical, and even biological processes, and finally achieve the power of prediction toward the engineering of new materials, for example, in photovoltaics.

Bibliography

[1] P. Hohenberg and W. Kohn. Inhomogeneous electron gas. *Phys. Rev.*, 136:B864, 1964.

[2] W. Kohn and L. J. Sham. Self-consistent equations including exchange and correlation effects. *Phys. Rev.*, 140:A1133, 1965.

[3] E. Runge and E. K. U. Gross. Density-functional theory for time-dependent systems. *Phys. Rev. Lett.*, 52:997, 1984.

[4] E. K. U. Gross and W. Kohn. Local density-functional theory of frequency-dependent linear response. *Phys. Rev. Lett.*, 55:2850, 1985.

[5] S. Kurth, G. Stefanucci, C.-O. Almbladh, A. Rubio, and E. K. U. Gross. Time-dependent quantum transport: A practical scheme using density functional theory. *Phys. Rev. B*, 72:035308, 2005.

[6] N. T. Maitra, T. N. Todorov, C. Woodward, and K. Burke. Density-potential mapping in time-dependent density-functional theory. *Phys. Rev. A*, 81:042525, 2010.

[7] T. K. Ng and K. S. Singwi. Time-dependent density-functional theory in the linear-response regime. *Phys. Rev. Lett.*, 59:2627, 1987.

[8] R. van Leeuwen. Key concepts in time-dependent density-functional theory. *Int. J. Mod. Phys. B*, 15:1969, 2001.

[9] M. Levy. Electron densities in search of Hamiltonians. *Phys. Rev. A*, 26:1200, 1982.

[10] H. Kohl and R. M. Dreizler. Time-dependent density-functional theory: Conceptual and practical aspects. *Phys. Rev. Lett.*, 56:1993, 1986.

[11] S. K. Ghosh and A. K. Dhara. Density-functional theory of many-electron systems subjected to time-dependent electric and magnetic fields. *Phys. Rev. A*, 38:1149, 1988.

[12] M Ruggenthaler, M. Penz, and R. van Leeuwen. Existence, uniqueness, and construction of the density-potential mapping in time-dependent density-functional theory. *J. Phys. Cond. Mat.*, 27:203202, 2015.

[13] R. van Leeuwen. Causality and symmetry in time-dependent density-functional theory. *Phys. Rev. Lett.*, 80:1280, 1998.

[14] M. Petersilka, U. J. Gossmann, and E. K. U. Gross. Excitation energies from time-dependent density-functional theory. *Phys. Rev. Lett.*, 76:1212, 1996.

[15] T. Ando. Inter-subband optical-absorption in space-charge layers on semiconductor surfaces. *Z. Phys. B*, 26:263, 1977.

[16] T. Ando. Inter-subband optical-transitions in a surface space-charge layer. *Solid. State. Commun.*, 21:133, 1977.

[17] A. Zangwill and P. Soven. Density-functional approach to local-field effects in finite systems: Photoabsorption in the rare gases. *Phys. Rev. A*, 21:1561, 1980.

[18] A. Zangwill and P. Soven. Resonant photoemission in barium and cerium. *Phys. Rev. Lett.*, 45:204, 1980.

[19] S. L. Adler. Quantum theory of the dielectric constant in real solids. *Phys. Rev.*, 126:413, 1962.

[20] N. Wiser. Dielectric constant with local field effects included. *Phys. Rev.*, 129:62, 1963.

[21] D. J. Thouless. Vibrational states of nuclei in random phase approximation. *Nucl. Phys.*, 22:78, 1961.

[22] D. J. Rowe. Equations-of-motion method and the extended shell model. *Rev. Mod. Phys.*, 40:153, 1968.

[23] M. E. Casida. Time-dependent density functional response theory for molecules. In D. E. Chong, editor, *Recent Advances in Density Functional Methods. Recent Advances in Computational Chemistry*, volume 1, page 155, Singapore, 1995. World Scientific.

[24] M. E. Casida. Time-dependent density functional response theory of molecular systems: Theory, computational methods, and functionals. In J. M. Seminario, editor, *Recent Developments and Application of Modern Density Functional Theory*, page 391, Amsterdam, 1996. Elsevier.

[25] A. Kono and S. Hattori. Accurate oscillator strengths for neutral helium. *Phys. Rev. A*, 29:2981, 1984.

[26] V. Olevano et al. http://www.dp-code.org, 2005-2017.

[27] X. Gonze et al. http://www.abinit.org, 1998-2017.

[28] J. K. Dewurst, S. Sharma, et al. http://elk.sourceforge.net/, 2017.

[29] M. A. L. Marques, A. Castro, G. F. Bertsch, and A. Rubio. Octopus: a first-principles tool for excited electron-ion dynamics. *Comput. Phys. Commun.*, 151:60, 2003.

[30] C. J. Umrigar and X. Gonze. Accurate exchange-correlation potentials and total-energy components for the helium isoelectronic series. *Phys. Rev. A*, 50:3827, 1994.

[31] M. Petersilka, E. K. U. Gross, and K. Burke. Excitation energies from time-dependent density-functional theory using exact and approximate potentials. *Int. J. Quant. Chem.*, 80:534, 2000.

[32] T. Burnus, M. A. L. Marques, and E. K. U. Gross. Time-dependent electron localization function. *Phys. Rev. A*, 71:010501, 2005.

[33] T. Burnus, M. A. L. Marques, and E. K. U. Gross. Time-dependent quantum transport: A practical scheme using density functional theory. *Phys. Rev. A*, 71:010501, 2005. Acetylene molecule excitation movie, Supplemental Material, http://journals.aps.org/pra/supplemental/10.1103/PhysRevA.71.010501/C2H2.mpeg.

[34] A. D. Becke and K. E. Edgecombe. A simple measure of electron localization in atomic and molecular systems. *J. Chem. Phys.*, 92:5397, 1990.

[35] T. Burnus, M. A. L. Marques, and E. K. U. Gross. Time-dependent electron localization function. *Phys. Rev. A*, 71:010501, 2005. Ethene molecule fragmentation movie, Supplemental Material, http://journals.aps.org/pra/supplemental/10.1103/PhysRevA.71.010501/C2H4.mpeg.

[36] A. Castro, M. A. L. Marques, D. Varsano, F. Sottile, and A. Rubio. The challenge of predicting optical properties of biomolecules: What can we learn from time-dependent density-functional theory? *C. R. Physique*, 10:469, 2009.

[37] D. R. Yarkony. Diabolical conical intersections. *Rev. Mod. Phys.*, 68:985, 1996.

[38] W. Domcke, D. R. Yarkony, and H. K. Noppel, editors. *Conical Intersections: Electronic Structure, Dynamics and Spectroscopy*. World Scientific, Singapore, 2004.

[39] L. Cederbaum. Born-oppenheimer approximation and beyond. In W. Domcke, D. R. Yarkony, and H. K. Noppel, editors, *Conical Intersections: Electronic Structure, Dynamics and Spectroscopy*, page 3. World Scientific, Singapore, 2004.

[40] J. Stiebling. Optical properties of mono-crystalline silicon by electron energy-loss measurements. *Z. Phys. B*, 31:355, 1978.

[41] Valerio Olevano. *Proprietà Dielettriche di Semiconduttori oltre l'Approssimazione di Densità Locale*. PhD thesis, Università di Roma "Tor Vergata", Rome, 1999.

[42] V. Olevano, M. Palummo, G. Onida, and R. Del Sole. Exchange and correlation effects beyond the LDA on the dielectric function of silicon. *Phys. Rev. B*, 60:14224, 1999.

[43] V. Olevano and L. Reining. Excitonic effects on the silicon plasmon resonance. *Phys. Rev. Lett.*, 86:5962, 2001.

[44] A. G. Marinopoulos, L. Reining, V. Olevano, A. Rubio, T. Pichler, X. Liu, M. Knupfer, and J. Fink. Anisotropy and interplane interactions in the dielectric response of graphite. *Phys. Rev. Lett.*, 89:076402, 2002.

[45] A. G. Marinopoulos, L. Reining, A. Rubio, and V. Olevano. Ab initio study of the optical absorption and wave-vector-dependent dielectric response of graphite. *Phys. Rev. B*, 69:245419, 2004.

[46] T. Eberlein, U. Bangert, R. R. Nair, R. Jones, M. Gass, A. L. Bleloch, K. S. Novoselov, A. Geim, and P. R. Briddon. Plasmon spectroscopy of free-standing graphene films. *Phys. Rev. B*, 77:233406, 2008.

[47] A. G. Marinopoulos, L. Wirtz, A. Marini, V. Olevano, A. Rubio, and L. Reining. Optical absorption and electron energy loss spectra of carbon and boron nitride nanotubes: A first principles approach. *Appl. Phys. A*, 78:1157, 2004.

[48] M. Bruno, M. Palummo, A. Marini, R. Del Sole, V. Olevano, A. N. Kholod, and S. Ossicini. Excitons in germanium nanowires: Quantum confinement, orientation, and anisotropy effects within a first-principles approach. *Phys. Rev. B*, 72:153310, 2005.

[49] P. E. Trevisanutto, C. Giorgetti, L. Reining, M. Ladisa, and V. Olevano. Ab initio GW many-body effects in graphene. *Phys. Rev. Lett.*, 101:226405, 2008.

[50] C. Kramberger, R. Hambach, C. Giorgetti, M. H. Rümmeli, M. Knupfer, J. Fink, B. Büchner, L. Reining, E. Einarsson, S. Maruyama, F. Sottile, K. Hannewald, V. Olevano, A. G. Marinopoulos, and T. Pichler. Linear plasmon dispersion in single-wall carbon nanotubes and the collective excitation spectrum of graphene. *Phys. Rev. Lett.*, 100:196803, 2008.

[51] H. C. Weissker, J. Serrano, S. Huotari, F. Bruneval, F. Sottile, G. Monaco, M. Krisch, V. Olevano, and L. Reining. Signatures of short-range many-body effects in the dielectric function of silicon for finite momentum transfer. *Phys. Rev. Lett.*, 97:237602, 2006.

[52] K. Sturm, W. Schülke, and J. R. Schmitz. Plasmon-fano resonance inside the particle-hole excitation spectrum of simple metals and semiconductors. *Phys. Rev. Lett.*, 68:228, 1992.

[53] U. Fano. Effects of configuration interaction on intensities and phase shifts. *Phys. Rev.*, 124:1866, 1961.

[54] W. Schülke, J. R. Schmitz, H. Schulte-Schrepping, and A. Kaprolat. Dynamic and static structure factor of electrons in Si: Inelastic x-ray scattering results. *Phys. Rev. B*, 52:11721, 1995.

[55] S. Huotari, J. A. Soininen, G. Vankó, G. Monaco, and V. Olevano. Screening in YBCO at large wave vectors. *Phys. Rev. B*, 82:064514, 2010.

[56] A. Mosca Conte, O. Pulci, M. C. Misiti, J. Lojewska, L. Teodonio, C. Violante, and M. Missori. Visual degradation in Leonardo da Vinci's iconic self-portrait: A nanoscale study. *Appl. Phys. Lett.*, 104:224101, 2014.

[57] M. Missori, O. Pulci, L. Teodonio, C. Violante, M. C. Misiti, I. Kupchak, J. Bagniuk, J. Lojewska, and A. Mosca Conte. Optical response of strongly absorbing inhomogeneous materials: Application to paper degradation. *Phys. Rev. B*, 89:054201, 2014.

[58] P. Lautenschlager, M. Garriga, L. Viña, and M. Cardona. Temperature dependence of the dielectric function and interband critical points in silicon. *Phys. Rev. B*, 36:4821, 1987.

[59] S. Albrecht, L. Reining, R. Del Sole, and G. Onida. Ab initio calculation of excitonic effects in the optical spectra of semiconductors. *Phys. Rev. Lett.*, 80:4510, 1998.

[60] M. S. Hybertsen and S. G. Louie. First-principles theory of quasiparticles: Calculation of band gaps in semiconductors and insulators. *Phys. Rev. Lett.*, 55:1418, 1985.

[61] R. W. Godby, M. Schlüter, and L. J. Sham. Quasiparticle energies in GaAs and AlAs. *Phys. Rev. B*, 35:4170, 1987.

[62] F. Sottile, M. Marsili, V. Olevano, and L. Reining. Efficient ab initio calculations of bound and continuum excitons in the absorption spectra of semiconductors and insulators. *Phys. Rev. B*, 76:161103(R), 2007.

[63] V. Saile, M. Skibowski, W. Steinmann, P. Gürtler, E. E. Koch, and A. Kozevnikov. Observation of surface excitons in rare-gas solids. *Phys. Rev. Lett.*, 37:305, 1976.

[64] Valerio Olevano. *Proprietà Dielettriche di Semiconduttori oltre l'Approssimazione di Densità Locale*. PhD thesis, Università di Roma "Tor Vergata", Rome, 1999. Pages 101 and 107.

[65] L. Reining, V. Olevano, A. Rubio, and G. Onida. Excitonic effects in solids described by time-dependent density functional theory. *Phys. Rev. Lett.*, 88:066404, 2002.

[66] S. Botti, F. Sottile, N. Vast, V. Olevano, H. C. Weissker L. Reining, A. Rubio, G. Onida, R. Del Sole, and R. W. Godby. Long-range contribution to the exchange-correlation kernel of time-dependent density-functional theory. *Phys. Rev. B*, 69:155112, 2004.

[67] S. Botti, A. Fourreau, F. Nguyen, Y.-O. Renault, F. Sottile, and L. Reining. Energy dependence of the exchange-correlation kernel of time-dependent density functional theory: A simple model for solids. *Phys. Rev. B*, 72:125203, 2005.

[68] R. Del Sole, G. Adragna, V. Olevano, and L. Reining. Long-range behavior and frequency dependence of exchange-correlation kernels in solids. *Phys. Rev. B*, 67:045207, 2003.

[69] F. Sottile, V. Olevano, and L. Reining. Parameter-free calculation of response functions in time-dependent density-functional theory. *Phys. Rev. Lett.*, 91:056402, 2003.

[70] G. Adragna. *Ab initio calculation of the TDDFT exchange-correlation kernel for semiconductors and insulators*. PhD thesis, Università di Roma "Tor Vergata", Rome, 2002.

[71] G. Adragna, R. Del Sole, and A. Marini. Ab initio calculation of the exchange-correlation kernel in extended systems. *Phys. Rev. B*, 68:165108, 2003.

[72] I. V. Tokatly and O. Pankratov. Many-body diagrammatic expansion in a Kohn-Sham basis: Implications for time-dependent density functional theory of excited states. *Phys. Rev. Lett.*, 86:2078, 2001.

[73] U. von Barth, N. E. Dahlen, R. van Leeuwen, and G. Stefanucci. Conserving approximations in time-dependent density functional theory. *Phys. Rev. B*, 72:235109, 2005.

[74] F. Bruneval, F. Sottile, V. Olevano, R. Del Sole, and L. Reining. Many-body perturbation theory using the density-functional concept: beyond the GW approximation. *Phys. Rev. Lett.*, 94:186402, 2005.

[75] M. Gatti, V. Olevano, L. Reining, and I. V. Tokatly. Transforming nonlocality into a frequency dependence: A shortcut to spectroscopy. *Phys. Rev. Lett.*, 99:057401, 2007.

[76] S. Sharma, J. K. Dewhurst, A. Sanna, and E. K. U. Gross. Bootstrap approximation for the exchange-correlation kernel of time-dependent density-functional theory. *Phys. Rev. Lett.*, 107:186401, 2011.

[77] V. U. Nazarov and G. Vignale. Optics of semiconductors from meta-generalized-gradient-approximation-based time-dependent density-functional theory. *Phys. Rev. Lett.*, 107:216402, 2011.

[78] V. U. Nazarov, G. Vignale, and Y.-C. Chang. Exact dynamical exchange-correlation kernel of a weakly inhomogeneous electron gas. *Phys. Rev. Lett.*, 102:113001, 2009.

[79] P. E. Trevisanutto, A. Terentjevs, L. A. Constantin, V. Olevano, and F. Della Sala. Optical spectra of solids obtained by time-dependent density functional theory with the jellium-with-gap-model exchange-correlation kernel. *Phys. Rev. B*, 87:205143, 2013.

[80] P. Elliott, S. Goldson, C. Canahui, and N. T. Maitra. Perspectives on double-excitations in TDDFT. *Chem. Phys.*, 391:110, 2011.

[81] N. T. Maitra. Perspective: Fundamental aspects of time-dependent density functional theory. *J. Chem Phys.*, 144:220901, 2016.

[82] K. Burke, J. Werschnik, and E. K. U. Gross. Time-dependent density functional theory: Past, present, and future. *J. Chem Phys.*, 123:062206, 2005.

[83] E. Luppi, H. Hübener, and V. Véniard. Ab initio second-order nonlinear optics in solids: Second-harmonic generation spectroscopy from time-dependent density-functional theory. *Phys. Rev. B*, 82:235201, 2010.

[84] M. Grüning, D. Sangalli, and C. Attaccalite. Dielectrics in a time-dependent electric field: A real-time approach based on density-polarization functional theory. *Phys. Rev. B*, 94:035149, 2016.